STRUCTURAL AND MAGNETIC CHARACTERIZATION OF $Li_xCo_{1-x}V_2O_4$ AND $Bi_{2-x}Se_3Co_x$

Thesis submitted to Sikkim University
for the partial fulfillment of the degree
of Masters of Philosophy in Physical Sciences(Physics).

Laden Sherpa
Roll No:14MPPY01
Regn. No:09SU1527

[A Central University Established By An Act Of Parliament Of India]

Department Of Physics
School Of Physical Science
SIKKIM UNIVERSITY
Tadong-737102
Gangtok,Sikkim
2016

सिक्किम विश्वविद्यालय
(भारतीय संसद के अधिनियमद्वारा स्थापित केन्द्रीय विश्वविद्यालय)
गुणवत्तापूर्ण प्रबंधन प्रणाली ISO 9001:2008 हेतु प्रमाणित संस्थान
SIKKIM UNIVERSITY
[A Central University established by an Act of Parliament of India in 2007]
An ISO Quality Management System 9001:2008 Certified Institution

DECLARATION

I declare that the thesis entitled "**Structural and Magnetic Characterization of $Li_xCo_{(1-x)}V_2O_4$ and $Bi_{(2-x)}Se_3Co_x$**" submitted by me for the award of **Master of Philosophy (M. Phil.) Degree in Physics** of Sikkim University is my original work. The content of this thesis is based on the experiments which I have performed myself. This thesis has not been submitted for any other degree to any other University.

Date: 20-06-2016

Laden Sherpa

Roll No: 14MPPY01

Regn. No: 09SU1527

We recommend that the thesis be placed before the Examiners for evaluation.

Supervisor

20/6/2016

Dr. Archana Tiwari

(Assistant Professor)

Department of Physics

Sikkim University

Head

20.6.16

Dr. Amitabha Bhattacharyya

(Associate Professor)

Department of Physics

Sikkim University

6 माईल, सामदुर, तादोंग, गंगटोक - 737102 सिक्किम, भारत
दूराभाष : 00-91-3592 - 251067, 251403, फैक्स :- 251067/251757
6th Mile, Samdur, PO Tadong 737102, Gangtok, Sikkim, India
Phones : 00-91-3592-251067, 251403, Fax - 251067/251757
website : www.sikkimuniversity.in/www.sikkimuniversity.ac.in
Email : sikkimuniversity@gmail.com

सिक्किम विश्वविद्यालय
(भारतीय संसद के अधिनियमद्वारा स्थापित केन्द्रीय विश्वविद्यालय)
गुणवत्तापूर्ण प्रबंधन प्रणाली ISO 9001:2008 हेतु प्रमाणित संस्थान
SIKKIM UNIVERSITY
[A Central University established by an Act of Parliament of India in 2007]
An ISO Quality Management System 9001:2008 Certified Institution

Certificate

This is to certify that the thesis entitled "**Structural and Magnetic Characterization of $Li_xCo_{(1-x)}V_2O_4$ and $Bi_{(2-x)}Se_3Co_x$**" submitted to Sikkim university in partial fulfillment of the requirements for the degree of **Master of Philosophy (Science) in Physics** embodies the result of *bona fide* research work carried out by **Miss Laden Sherpa** under my guidance and supervision. No part of the thesis has been submitted for any other degree, diploma, associate-ship, fellowship.

All the assistance and help received during the course of the investigation have been duly acknowledged by her.

Archana Tiwari

(Dr. Archana Tiwari)

M. Phil. Supervisor

Department of physics

School of Physical and Chemical Sciences

Place: Gangtok

Date: 20/06/2016

6 माईल, सामदुर, तादोंग, गगंटोक - 737102 सिक्किम, भारत
दूराभाष : 00-91-3592 - 251067, 251403, फैक्स :- 251067/251757

6th Mile, Samdur, PO Tadong 737102, Gangtok, Sikkim, India
Phones : 00-91-3592-251067, 251403, Fax - 251067/251757
website : www.sikkimuniversity.in/www.sikkimuniversity.ac.in
Email : sikkimuniversity@gmail.com

STRUCTURAL AND MAGNETIC CHARACTERIZATION OF $Li_xCo_{1-x}V_2O_4$ AND $Bi_{2-x}Se_3Co_x$

Thesis submitted to Sikkim University
for the partial fulfillment of the degree
of Masters of Philosophy in Physical Sciences(Physics).

Laden Sherpa
Roll No:14MPPY01
Regn. No:09SU1527

[A Central University Established By An Act Of Parliament Of India]

Department Of Physics
School Of Physical Science
SIKKIM UNIVERSITY
Tadong-737102
Gangtok,Sikkim
2016

Acknowledgement

Firstly, I would like to express my sincere gratitude to my supervisor Dr. Archana Tiwari for her continuous support during my M.phil. research work. I want to thank her for her patience, immense knowledge and guidance in all times of research and writing of this thesis. I could not have imagined having a better mentor for my M.Phil. course.

I would like to thank Dr.Ajay Tripathi for his guidance in Mathematica programming and his insightful comments and encouragement which helped me to widen my research from various perspectives. My sincere thanks also goes to Dr. Subir Mukhopadhyaya, Dr. Amitabh Bhattacharyya, Dr. Dhurba Rai and Dr. Hemam Dinesh Singh for their encouragement.

I would like to express my especial gratitude to Dr. Prashant Sahi, Dr. Ranjan Kr. Singh and Dr. Sandip Chatterjee of Department of Applied Physics, IIT BHU for providing the samples. Without which I would not have been able to do my research work. I wish to acknowledge Dr. Chandan Mukherjee, Department of Chemistry IIT Guwahati for providing the EPR measurements data. Dr. Somendra chakraborty, Department Of Chemistry Sikkim University for his support during the X-ray diffraction measurements.

I would also like to thank Mr. Binod Chettri lab attendant of Department of Chemistry, Sikkim University for his patience and guidance during all of my XRD measurements. Mr. Vikram Thapa lab attendant of Department of Physics, Sikkim University for helping me whenever needed. I thank all of my friends from computer lab for the stimulating discussions, for the times when we were working together before deadlines, and for all the fun we have had in the two years.

Last but not the least, I would like to thank my family: my parents and to my sister for supporting me spiritually throughout writing this thesis and my life in general. I would like to dedicate this thesis to my mother, my role model of strong and independent woman.

Abstract

A suitable transition metal dopant in the matrices of spinel oxides and topological insulators are known to tune their structural, magnetic and transport properties. The impact of Li dopant in vanadium spinel oxide $Li_xCo_{1-x}V_2O_4$ and Co dopant in $Bi_{2-x}Se_3Co_x$ insulators has been studied. They exhibit interesting structural and magnetic properties. In spinel oxide such properties arise from the arrangement of octahedral and tetrahedral environment of AB_2O_4 and interaction between spin charge and orbital degrees of freedom. The non-magnetic Li dopant is added in vanadium spinel oxide of formula AB_2O_4 where Co^{2+} occupies the tetrahedral A site and V^{3+} occupies the octahedral B site. On the other hand topological insulators are class of materials which has time reversal symmetry and band gap in the bulk but the gapless states on the surface. The surface states are immune to defects and non-magnetic disorder. A magnetic impurity like transition metal ion in it leads to modification of such surface states. Bi_2Se_3 has emerged as the most interesting three dimensional topological insulator[1]. The magnetic impurity Co acts as perturbation on the surface of $Bi_{2-x}Se_3Co_x$ topological insulator. It breaks the time reversal symmetry and opens the energy gap. The change in the properties of $Li_xCo_{1-x}V_2O_4$ and $Bi_{2-x}Se_3Co_x$ due to dopant is classified into two categories viz. structural and magnetic properties. The interference of dopant with the crystal environment is seen as an initiation of lattice distortion, spin-orbit coupling influencing the structural and magnetic properties.

The observations of the structural properties on doped samples with the undoped CoV_2O_4 and Bi_2Se_3 shows the crystal lattice parameter changes for different concentration of dopant ion as revealed from XRD measurements. The inclusion of dopant ion interfered with the phonon vibrations which is identified from vibrational spectroscopy like Raman and FTIR. The crystal structure as a whole remain unperturbed on doping. The magnetic interaction in the sample were studied by obtaining hysteresis curve and EPR spectra at room temperature,300K and low temperature,80K. The hysteresis curve show the samples are ferromagnetic at both the temperatures. On doping of external ion the change in magnetic behaviour is interpreted in terms of their coercivity, H_c and remnant magnetization M_r. At 300K and 80K the parameters of hysteresis curve reveals the ferromagnetic interaction in CoV_2O_4 and Bi_2Se_3 is weak at 300K. It is supported by the EPR measurements which reveals the presence of paramagnetic interaction at 300K while no such interaction is observed at 80K. The mathematical simulation of magnetic hysteresis at 300K is performed using the Stoner-Wohlfarth(SW) model for a single magnetic domain. The orientation of magnetic field with respect to anisotropy axis (α) and anisotropy field, H_k of CoV_2O_4 and Bi_2Se_3 are identified. An easy spin spectral simulation is also performed at 300K, an isotropic anisotropy in CoV_2O_4 and paramagnetic interaction of spin 1/2 system for $g>g_e$ is observed. The anisotropy is changed to uniaxial anisotropy in $Li_xCo_{1x}V_2O_4$ upon doping. In Bi_2Se_3 the paramagnetic interaction is not observed for the undoped Bi_2Se_3 while upon doping $Bi_{2-x}Se_3Co_x$ posses a uniaxial anisotropy.

Contents

List of Figures

Part I

Chapter 1

Introduction

Introduction

Spinel oxides exhibit fascinating and wide range of physical, electrical, optical and magnetic properties. These properties depend on the crystal environment and external factors like temperature and pressure[2]. A dopant in a crystal matrix of a spinel vanadium oxide acts as a perturbation in the crystal environment. Upon doping the properties can be modified. Doping the matrices with metal or non-metal ion give rise to entirely different properties[3]. The tunability of properties depend on the selection of the dopant ion. The doped materials like ZnO, NiO, FeV_2O_4 display structural orientation and magnetic properties strongly influenced by external dopant in their crystal matrix[4, 5]. They exhibit specific crystal structure depending on the composition. For example, in spinel oxide a combination of tetrahedron and octahedron crystal environments are found. In spinel oxides tetrahedron is coordinated by four oxygen neighbors while octahedron is co-

ordinated by six oxygen neighbors. In spinel vanadates AB_2O_4 arrangement is seen. The A site is a divalent cation transition metal ion and B site is trivalent Vanadium ion[6, 7]. $Li_xCo_{1-x}V_2O_4$ is a spinel oxide where a non magnetic Li ion is doped. CoV_2O_4 comprises of Co^{2+} and V^{3+} ions at A site and B site with orbital degrees of freedom only at B site. The interest on such material is driven by its quality interaction of spin, charge and orbital degrees of freedom which are essentially desired for soft magnetic application e.g. high permeability, low coercivity, low core loss etc [6].

The topological insulators are a class of materials which are composed of heavy elements like Bi, Te, Se, Sb etc. The bulk of such material is an insulator but the surface has conducting states. The spin orbit interaction present in the material modifies the unoccupied and occupied states in a way that the energy levels are inverted. The high energy levels appear below band gap while the low energy bands appear above the band gap giving rise to highly conducting metallic surface[8]. A topological insulator has a time reversal symmetry. The surface is protected and remains unaltered by some ordinary defects or a non-magnetic disorder. The heavy-element, small-band gap semiconductors are the most promising candidates for topological insulator as they show strong spinorbit coupling. Also if the band gap of the selected material is much larger than the energy scale of spinorbit coupling, then the energy levels cannot be modified[9]. Bi_2Se_3 is a chemically stable compound which exhibits robust topological phase. Studies on these transition metal ion-doped topological insulator are motivated by various interesting phenomena such as quantized anomalous Hall effect, magnetic monopole and giant-magneto-optical effects. The interest is on finding a way to break time

reversal symmetry on their surface. Such properties have several practical application in spintronics and quantum computation[10, 11].

My research focuses on presenting the change in the properties of the given spinel oxides and the topological insulator upon changing the doping concentration. Spinel oxide $Li_xCo_{1-x}V_2O_4$ and topological insulator $Bi_{2-x}Se_3Co_x$ have been used. To observe the modification, versatile spectroscopic techniques have been used for structural and magnetic characterization. The changes in the properties are studied as reflection due to the interplay between the orbital and the spin degrees of freedom, exchange interactions, substitution of ions, coulomb repulsion, lattice defects etc. of the materials[12]. Further the numerical simulation based on Stoner-Wohlfarth model and spectral simulation easyspin is performed to support the magnetic characterization of the samples.

1.1 Objective

The objective of this work is to understand the effect of dopant on spinel oxide and topological insulator class of material. For this the following materials were chosen.

- Li doped spinel vanadium oxide($Li_xCo_{1-x}V_2O_4$)
- Co doped topological insulator($Bi_{2-x}Se_3Co_x$)

We have studied the structural morphology and their magnetic behaviour. In the interest of tuning the properties of spinel oxide and TI, this study focuses on the effects of doping in the above samples. The work records the change in the properties of the samples by characterising them structurally and magnetically using various spectroscopic techniques. It shall enable one to understand the structural and electronic modifications in the sample upon being doped by an external ion. The experimentally obtained magnetometric measurements are further analyzed using numerical and spin simulation. Stoner-Wohlfarth model considers a ferromagnetic material with a single domain and is used for regenerating the magnetic hysteresis loop of the samples. While easy spin simulation is used for spectral simulation of spin and its interaction with the magnetic field and the environment. The spin properties of the material and g values are determined. This study helps in understanding the effects of dopants on structural and magnetic properties of the samples by investigating their lattice parameter, modes of vibrations and the prevalent magnetic interaction and anisotropy in the identified samples.

1.2 Outline of thesis

The structural and magnetic properties are studied in doped spinel oxide $Li_xCo_{1-x}V_2O_4$ and topological insulator $Bi_{2-x}Se_3Co_x$.

In **chapter 1**a brief introduction of the spinel oxide and topological insulator and effect of doping on such materials is given. The objective of the work is also presented.

In **chapter 2**the structural and magnetic properties of the spinel oxide CoV_2O_4 and topological insulator Bi_2Se_3 doped is reviewed. Also the changes reported with dopant are also reviewed. The basics of magnetization and Stoner-Wohlfarth model are discussed.

In **chapter 3**the materials and the spectroscopic techniques utilized for the structural and magnetic characterization that were used in our study is introduced.

In **chapter 4**the results obtained by doping of Li ion in CoV_2O_4 sample is discussed. Both the structural and magnetic characterization is presented. Also the magnetic data is further explained using SW model and easyspin software.

In **chapter 5**results obtained upon doping of Co ion in Bi_2Se_3 sample is discussed. Its structural and magnetic characterization is interpreted. The

magnetic hysteresis loop and EPR spectra are simulated using simple SW model and easyspin software.

In **Chapter 7**the conclusion and future prospects of the work with the scope of its application in the field of science is given.

Chapter 2

Review of Literature

2.1 Introduction

The substantial application of the doped spinel oxides and the topological insulators in the condensed matter and applied physics is the main motivation of the present work. This work examines the changes in the samples under investigation by varying the concentration of the dopant in the given matrices. There have been various studies upon doped materials in search of appropriate materials for different applications [1, 13, 14]. Such studies include application in the field of spintronics, magnetic storage devices etc.[15]. The dopant in spinel oxide and topological insulator has so much to offer as it provides wide range of possibilities to the researchers to discover advanced materials on the basis of parameters like composition, temperature, pressure, electric and magnetic fields. Doped metal oxide gained importance in 1950 when Wollan et.al reported that by varying the concentration of Ca in $La_{1-x}Ca_xCuO_4$ its properties can be tuned. Later the discovery of high

temperature superconductivity in $La_{2-x}Ba_xCuO_4$ in 1986 led to strong fascination in metal oxides[2]. Since then there are many findings like the giant entropy change in wide temperature range of 10-80K or <250K in $Gd_5Si_2Ge_2$, $MnAs_{1-x}Sb_x$, $MnFeP_{1-x}As_x$ and $La_{0.62}Bi_{0.05}Ca_{0.33}MnO_3$ which has potential application in magnetocaloric materials[16, 17]. The diluted magnetic semiconductors and room temperature ferromagnetism found in transition metal ion doped ZnO, has grabbed much attention for designing spintronics materials as they have several advantages over the charged based devices in data processing[18, 19]. However the materials required for these practical application have inevitable limitation due to their high cost. This is why the major interest is to fabricate material with low cost composition[3].

Materials like Bi_2Se_3 and Bi_2Te_3 were known as the traditional thermoelectric materials which can directly convert heat waste to electricity without any mechanical action. They are largely used as thermoelectric refrigeration. In the 1980s it was discovered that the electrons confined in two dimensions placed in a strong magnetic field showed a different, topology giving rise to quantum Hall effect at a very low temperature. In the past few years it was discovered that such topological order also occurred in three-dimensional materials. Such materials were known as topological insulator. In these materials, the magnetic behaviour is due to the mechanism of spinorbit coupling, an intrinsic property of all solids. Topological insulator can be described as an insulator that always has a metallic boundary when placed next to a vacuum or an ordinary insulator[8, 9, 20]. Bi_2Se_3 is an example of topological material. To understand the fascinating macroscopic properties one must look into the microscopic properties.

2.2 Spinel Oxide

Spinel oxides are generally of the formula AB_2O_4. The A and B sites are occupied by some transition metal ion. The A site is any divalent cation transition metal ion coordinated tetrahedrally with the four ligand oxygen. The B site e.g. in spinel vanadate is a trivalent Vanadium ion coordinated octahedrally with the six oxygen neighbor. The crystal structure of AB_2O_4 is polycrystalline in nature. It is combination of tetrahedron AO_4 and the octahedron BO_6 structure. The schematic illustration of a common spinel oxide AB_2O_4 is shown in Fig. 2.1, where the octahedral BO_6 and tetrahedral AO_4 gives rise to its crystal structure. The nature of such spinel oxides and

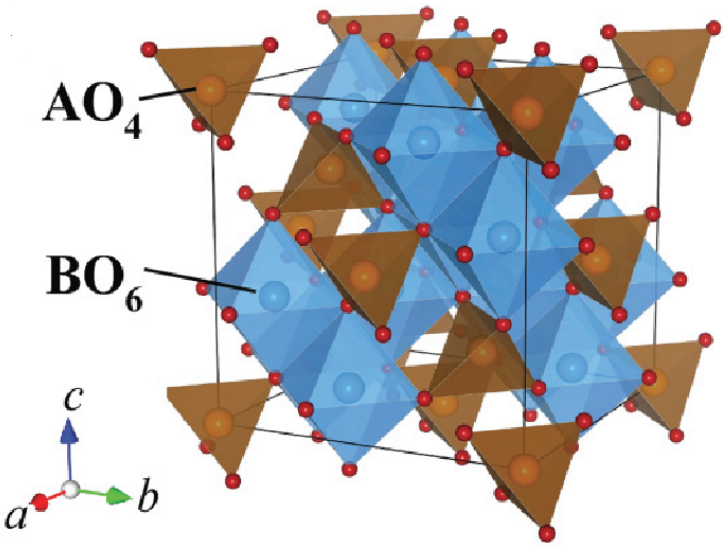

Figure 2.1: Schematic illustration of spinel oxide[4].

their properties are well explained by crystal field theory.

2.2.1 Crystal field theory

A crystal field is the environment of the constituent metals and the oxides where the transition metal is surrounded by the oxygen atoms. The crystal field theory suggests the neighboring atoms as a negative point charges. The field arises due to the electrostatic repulsion from the negatively charged electron of the ligand oxygen. These interaction of transition metal and the coordinating oxides affect the energy levels of the metal oxides. The d orbital of the transition metal, p orbital of the neighboring oxygen and their overlap defines the energy level of the system. The d orbital are classified into two types viz. e_g and t_{2g}. e_g is doubly degenerate orbital. t_{2g} is a triply degenerate orbital. The doubly degenerate e_g orbital are d_{z^2} and $d_{x^2-y^2}$. The symmetry of d_{z^2} lies along the Z axis and $d_{x^2-y^2}$ lies in the plane of X,Y axes. Similarly the triply degenerate t_{2g} are d_{xy}, d_{yz}, d_{zx}. All the three t_{2g} orbital lie in the plane of XY, YZ and ZX axes as shown in Fig. 2.3.

The overlap of these degenerate d orbitals with the p orbital of the ligand oxygen will redefine the energy level of the degenerate orbitals. In Fig. 2.3 the octahedral environment is considered. The overlap of the degenerate d and the ligand p orbital has been shown. Fig. 2.3 (a) shows the placement of $d_{xy}(t_{2g})$ orbital which do not overlap with the p orbital. Thus placing orbital t_{2g} in the lower energy level as shown in Fig. 2.3 (c). In Fig. 2.3 (b) the overlap of the $d_{x^2-y^2}(e_g)$with the p orbital is shown. The overlap places orbital e_g in higher energy level. If the environment considered had been a tetrahedral environment then the energy level would be reversed making t_2g the higher level and e_g the lower level. The electronic configuration of

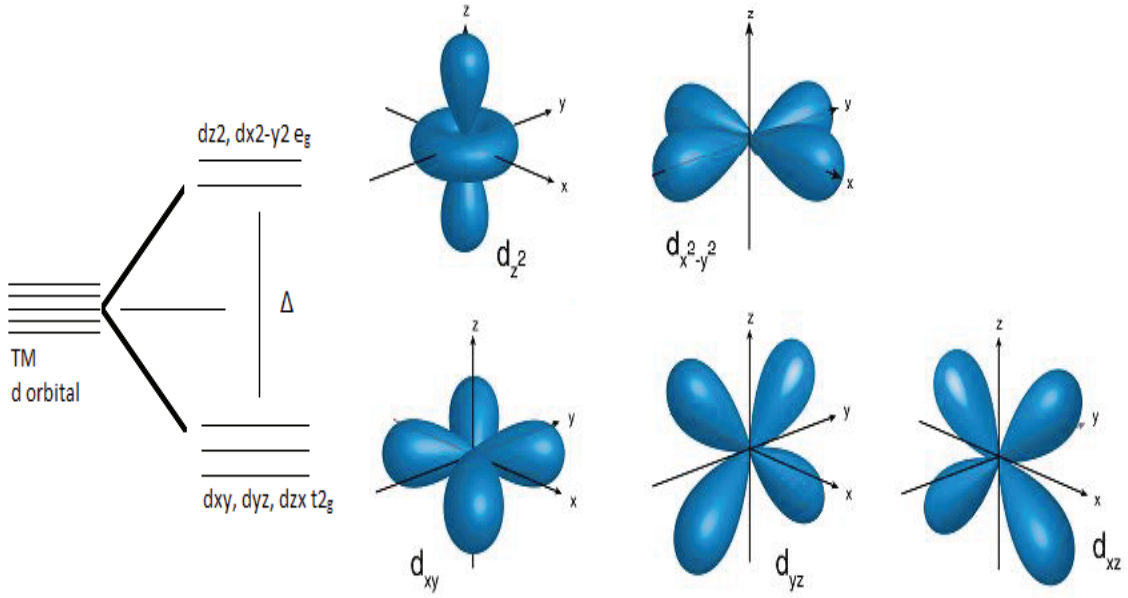

Figure 2.2: Types of D orbital

these levels result from the competition between crystal field energy and the pairing energy. The competition in configuration process leads to strong and weak field cases. In weak field case where the crystal field energy is weaker than the pairing energy, the electron will be distributed as per Hund's rule. In strong field case the electron first finish populating the first orbital before moving to next. The filling process determines the spin configuration. For weak field case we have high spin configuration and for strong field case it is low spin configuration Fig. 2.4[7].

The configuration largely influences the crystal's structural and magnetic properties[4]. In general the changes in the properties are reflected due to the interplay between the spin orbit coupling, exchange interactions, substitution of ions, coulomb repulsion, lattice defects etc[12].

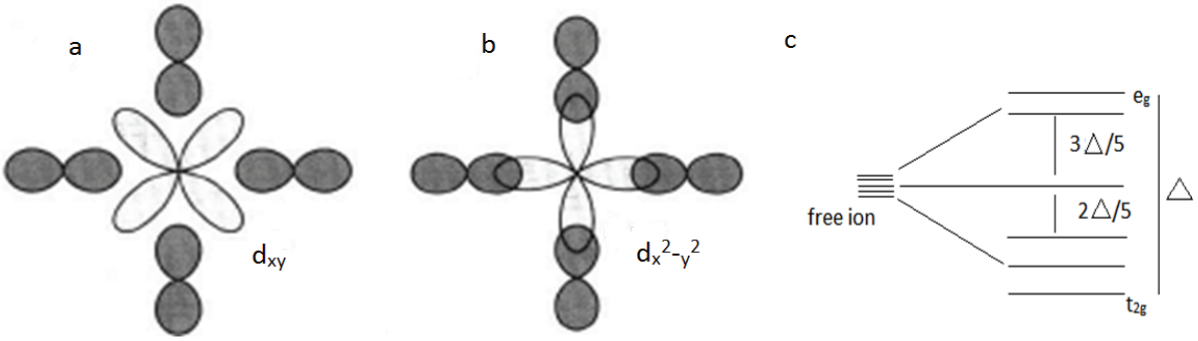

Figure 2.3: Overlap of the degenerate d orbitals(a)t_{2g} d_{xy} (b)e_g $d_{x^2-y^2}$ with the p orbitals in a octahedral environment and (c)redefined energy level[7].

AV_2O_4 where A= Mn, Zn, Fe and Co

In MnV_2O_4, the A site is occupied by Mn^{2+} and resides in a tetrahedral environment. It has $3d^5$ configuration and there is no orbital degrees of freedom as the d orbital is half filled and S=5/2 is the high spin configuration. The V^{3+} has $3d^2$ electrons which resides in the t_{2g} orbital of the octahedral environment. It has orbital degrees of freedom and S=1 is the high spin configuration. In this material both structural and magnetic properties changes under the variation of temperature. It is reported that the exchange interaction between Mn^{2+} and V^{3+} mediated by oxygen in MnV_2O_4 leads to ferrimagnetic ordering at the Neel's temperature T_N=56K[4, 12]. A structural phase transition occurs from cubic to tetragonal at a temperature T_S=53K[21]. The change in structural and magnetic properties implies to the fact that the magnetic and elastic behaviour are related. A crystal can deform itself while lowering the anisotropy energy, such deformation to save energy is also called Jahn-Teller effect[7]. When the system is in a ferrimagnetic state a ferromagnetic configuration of Vanadium spin occurs. It changes the orbital-

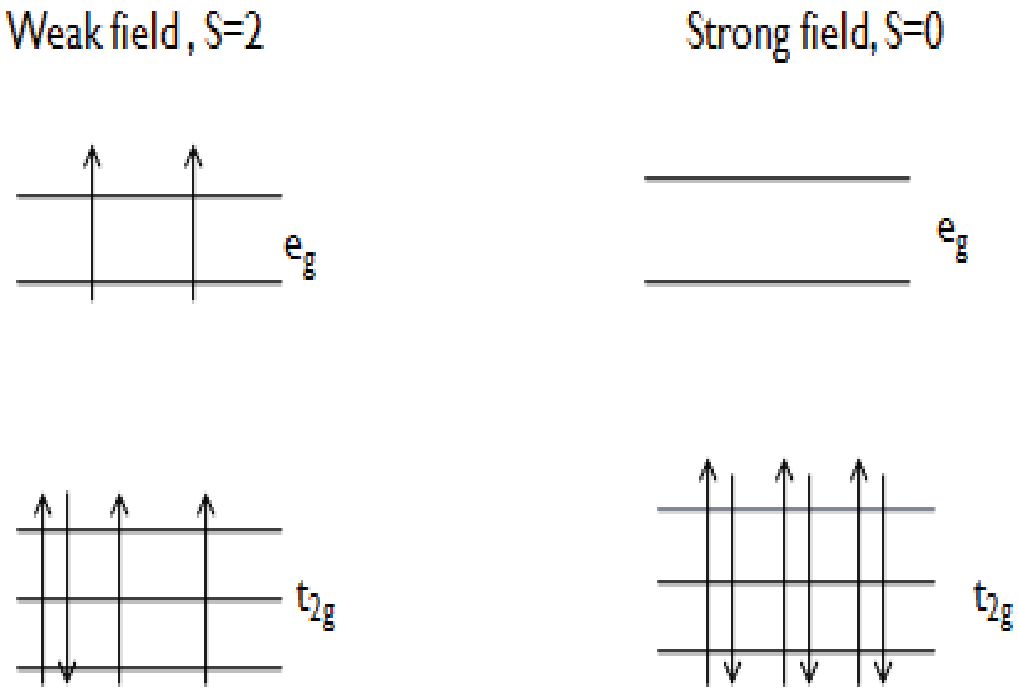

Figure 2.4: The high and low spin configuration in the crystal environment[7].

orbital interaction between neighboring V sites. This configuration results in the orbital ordering and therefore structural phase transition at T_S. Therefore the spin-orbit coupling in MnV_2O_4 is driven by magnetic-ordering. The observed magnetic field switching of crystal structure can also be explained similarly. When a magnetic field is applied, the ferromagnetic configuration of V spins occurs at higher temperatures, and accordingly the orbital ordering or structural phase transition occurs at higher temperatures[4, 21]. The replacement of Mn metal ions by some other metal ions can give rise to a different property. When the Mn^{2+} in A site of AV_2O_4 is replaced by Fe, the

doubly degenerate e_g orbital at A site will have orbital degrees of freedom. The configuration of electrons becomes $3d^6$ with spin S=2.

In FeV_2O_4 it is reported that the structural phase transition from cubic to tetragonal occurs at T_S=140K[3]. This transition is attributed to the Jahn-Teller interactions of FeO_4 in the tetrahedral environment. Jahn-Teller interaction here distorts the environment to balance the overall energy of the system. The presence of orbital degrees of freedom and high spin configuration results in strong spin orbit coupling. This spin orbit coupling in Fe^{2+} ion leads to ferrimagnetic ordering at T_N=110K. Also a structural transition from tetragonal to orthorhombic and vice versa at 70 K is reported in this material[19, 22]. It is noteworthy that T_S reported in FeV_2O_4 is higher than T_N which is opposite in MnV_2O_4. Therefore in FeV_2O_4 the spin-orbit coupling is structural-ordering driven one. Other then FeV_2O_4 and MnV_2O_4 structural and magnetic transitions is seen in spinel oxides ZnV_2O_4. It has been reported that a structural transition from cubic to tetragonal phase transition occurs at low temperature T_S=50K[13]. Also an antiferromagnetic ordering takes place at T_N=40K. Depending upon the nature of the metal or a non-metal ion the properties varies significantly. In spinel oxide CoV_2O_4 the temperature dependence study shows a paramagnetic-to-ferrimagnetic transition at T_C = 142K along with phase transitions at 59K and 100K. The transitions are predicted to be caused as a result of magnetic transitions due to the short range orbital order at V^{3+} sublattice. Such ordering of orbitals enhances the anti-ferromagnetic interaction among V^{3+} sites. Also no stuctural transition is observed on CoV_2O_4 which is predicted due to the weak JT effect and the orbital fluctuations for V^{3+}[23].

The phase transitions in the spinel oxides are still controversial in spite of extensive theoretical studies. It can be due to the poorly separated interaction like Jahn-Teller, spin orbit, and magnetic interactions which have energy of same scale. In general the structural transition T_S is proposed to be driven by effects like Jahn-Teller interaction which lifts the degeneracy of the spin-singlet local ground states at each tetrahedron unit of the pyrochlore lattice but it fails to explain the ordering at T_N[14]. Also the orbital order induces modulation of the spin-exchange coupling depending on the bond direction. This partially releases the frustration and leads to a spin order observed at $T_N = 40K$.

2.3 Topological Insulators

Other than oxides, Bi_2Se_3 is a good thermo electric material which has attracted more attention as a topological insulator as they have exciting fundamental properties. They have unusual insulating band gap and have strong spin orbit coupling which gives rise to topologically protected surface states. Its structure is made up of a few quintuple layers. Each basic unit cell has five layers of ordered as three Se-Bi-Se-Bi-Se sequence making a covalent bond. The layers are bonded by weak Van der waals force. The thickness of each layer is about 0.96 nm[24, 25]. It is a narrow band gap semiconductor and its calculated band gap is approximately 0.2eV with the measured value between 0.2eV-0.3eV[26]. It is highly anisotropic and studies show that the topological insulator in nanoscale show enhanced topology and surface conduction than the bulk. This occurs because the surface to volume ratio is

larger in nanoscale[27][28]. Bi_2Se_3 has a rhombohedral crystal structure that can be represented as a hexagonally stacked arranged atomic planes,each consisting of only one type of atom. The rhombohedral unit cell comprises of fcc close-packed five atomic layers (SeBiSeBiSe) along the crystallographic axis. Each Bi or Se layer within the quintuple layer has a two-dimensional hexagonal lattice perpendicular to the crystallographic axis[29, 30, 31]. The stacking of the Bi_{23} atoms is shown in Fig. 2.5.

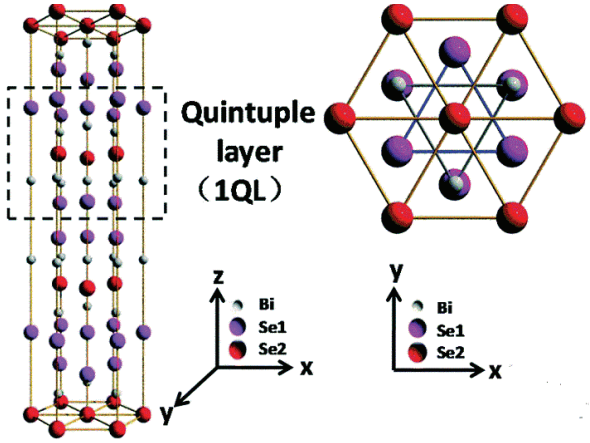

Figure 2.5: Layered crystal structure of Bi_2Se_3, with each quintuple layer (QL) stacking in the SeBiSeBiSe sequence along the z axis and Top view of the schematic Bi_2Se_3 structure.

The materials like Bi_2Se_3, Sb_2Te_3 etc. have layers bonded by weak van der Waals force. They are classic room temperature thermoelectric material. The layered compounds have interlayer coupling which affects its electronic structure. Even a small value of the elastic constant associated with the weak interlayer coupling results in strong variation of the valence band electronic structure with temperature, external pressure, or chemical pressure. There is a strong electron-phonon coupling associated with interlayer distance variation of these materials[30]. Temperature dependent variation in

Bi_2Se_3, Sb_2Te_3 crystals show the materials are capable of thermal expansion and change in size and shape on heating and cooling. The linear thermal expansion coefficients in the range of 10K-270K were found consistent with the Debye model at low temperatures. The temperature which breaks the van der Waals bond is predicted as the deviation in linear thermal expansion and is observed above 150K[32]. The study of Co doped Bi_2Se_3 show the magnetic susceptibility changes from diamagnetic to paramagnetic at room temperature.The magnetic study at 2K show ferromagnetic behaviour which varies with the Co concentration. The lower dopant concentration of cobalt in $Bi_{2-x}Se_3Co_x$(x=0.1, 0.15, 0.2) resulted in a simple metallic behavior whereas higher doping concentration like $Bi_{1.8}Se_3Co_{0.2}$ showed Kondo effect below 40K. Above 40 K the interactions between the local spins of cobalt ions and conduction electrons becomes weak. Kondo effect is the magnetic interaction of the electrons in a conductor. The semiconducting behavior is also been reported in $Bi_{1.8}Se_3Co_{0.2}$ at temperature below 40K[30, 1]. It is observed the bulk carrier concentration of $Bi_{1.8}Se_3Co_{0.2}$ is too high but the transport measurements carried out on nano-devices of same material shows the suppression of bulk topology. Such suppression in $Bi_{1.8}Se_3Co_{0.2}$ due to the magnetic impurities shows the breaking of time reversal symmetry in the material[1].

2.4 Stoner-Wohlfarth model

Ferromagnetic materials are divided in small regions called domains. The domains have the different orientation of magnetization from each other. When a external magnetic field is applied to a ferromagnetic material a magnetization takes place. The value of the output magnetization M versus the input applied field H can be plotted and the projection is called the magnetic hysteresis loop. A hysteresis loop is characterized by the saturation magnetization M_s, the remnant magnetization M_r and the coercive field(or coercivity) H_c. The mathematical model are used to study the hysteresis curves of materials, few of the mathematical models are Stoner-Wohlfarth model(SW), Tellinen model, Preisach model [33] etc. In this study we have used the SW model of ferromagnetism. It is the simplest model which describes the physics of tiny magnetic grains containing single magnetic domains[34, 35, 36]. To understand the insight of magnetism in magnetic materials the SW model considers the particles to have single domain, a uniform magnetization within and uniaxial anisotropy favouring magnetization along one particular direction.

2.4.1 Magnetic domain and anisotropy

The magnetic behaviour of the materials can be broadly classified into three types, diamagnetic paramagnetic and ferromagnetic. A diamagnetic substance placed in a magnetic field induces a magnetic moment which opposes the applied field that caused it. All materials show some degree of diamagnetism in them. Paramagnetic materials under applied magnetic field induces

a magnetic moment which are aligned in the direction of the magnetic field. In such materials no induced magnetic moment is present in absence of magnetic field. In ferromagnetic materials the induced magnetic moment persists even after the removal of the applied magnetic field. The Hamiltonian for ferromagnets is given by

$$H = -\sum_{i \neq j} J_{ij}.S_i.S_j + g\mu_B \sum S_j.B$$

The first term is the Heisenberg exchange energy where the sum is carried out over all spin pairs of nearest neighbours, J is the exchange integral, and S is the spin vector. Exchange interaction is a quantum-mechanical phenomenon that gives the energy of two elementary particles. Exchange is due to Pauli Exclusion Principle and Coulomb repulsion. In accordance with the Pauli Exclusion Principle, electrons obey Fermi-Dirac statistics; that is, only one electron can occupy a discrete quantum state at a time. When atoms are placed close together as they are in a crystal, the electron wave functions of adjacent atoms may overlap. The resultant wave function will be either symmetric or antisymmetric. Here, it is found that given a certain direction of magnetization for one atom, the energy of the second atom is higher for one direction of magnetization than the other. This difference in energy between the two states is called exchange energy. Furthermore, when the parallel magnetization is the lower energy state, the exchange is said to be ferromagnetic, but when the antiparallel magnetization is the lower energy state, the exchange is said to be antiferromagnetic[37]. The second term is the Zeeman energy. In external magnetic field the atomic energy levels splits

into a larger number of levels called as the Zeeman splitting. The energy difference between these two split states is called the Zeeman energy. Ferromagnets consists of domains within which the local magnetization reaches its saturation value[7]. The whole material is distributed into the domains which are separated by domain walls. The presence of domains explains why ferromagnets has spontaneous magnetization even in absence of magnetic field. The magnitude of magnetization M for the entire solid is a vector sum of magnetization in all domains. The domain walls are classified into two types Bloch wall(180^o) and Neel wall(90^o). The classification is based on the angle made by rotation of magnetization between two neighboring domains. The domains with Bloch walls have magnetization that rotates in the plane parallel to the wall separating domains of opposite magnetization while the magnetization rotating in a plane perpendicular to the domain wall are Neel walls separating domains of perpendicular magnetization. Bloch walls are common in bulk materials as it reduces the energy resulting from the interaction of magnetic moments with each other while Neel walls are favoured in thin films. The factors affecting the domains of a ferromagnetic material are dipolar energy, exchange energy and anisotropy energy. The dipolar energy is the energy due to the interaction of magnetic moments inside the domains that produces a demagnetizing field and also known as demagnetizing energy. A magnetic material has magnetic free poles at the surface which are enough to generate demagnetizing field or dipolar energy when placed in an external field. Such dipolar energy can be reduced by breaking the material into number of domains. Because ∇.H=-∇.M so the magnetic field diverges at the edges of a sample and produces demagnetizing fields. Thus

the demagnetizing energy can be reduced if the sample is broken into smaller domains. Anisotropy energy arises from the spin-orbit interaction and the partial quenching of the angular momentum. The magnetic anisotropy energy is defined as the energy that is necessary to turn M into any direction different from the preferred axes. If the magnetic moments in a material have a bias towards one particular direction then the material is said to have uniaxial anisotropy[38]. Anisotropy energy is directionally specific and is larger in low symmetry and smaller in high symmetry of crystals. The formation of domain costs energy but it also saves demagnetizing energy produced when the magnetic field diverges at the edges of the material. In the same way the width of a domain wall is a balance between the exchange and anisotropy energies[7, 39]. When the magnetic moments are aligned towards the crystal axis the anisotropy energy becomes less which reduces the width of the wall while the width increases when the moments lie parallel to each other reducing the exchange energy. Anisotropic energies depend on the structure and shape of the material. The magnetic anisotropy in SW model includes magnetocrystalline energy and shape anisotropy only. Magnetocrystalline anisotropy is an intrinsic property of a ferromagnets which arises from the spin-orbit coupling of spin magnetic moment and crystal lattice. A material is said to have magnetocrystalline anisotropy if it takes more energy to magnetize a crystal in certain directions (hard axis)than in other directions(easy axis). The magnetocrystalline energy density can be written as power series

of expansion of the magnetization, for cubic symmetry

$$\begin{aligned} E_{crys} &= K_0 + K_1 sin^2\alpha + K_2 sin^4\alpha + .. \\ E_{cubic}(\overrightarrow{M}, \overrightarrow{H}) &= K_0 + K_1(\alpha_1^2\alpha_2^2 + \alpha_2^2\alpha_3^2 + \alpha_1^2\alpha_3^2) + K_2\alpha_1^2\alpha_2^2\alpha_3^2 + H(\alpha_1\beta_1 + \alpha_2\beta_2 + ..) \end{aligned}$$

where α and β are direction cosines of unit vectors.

For hexagonal structures the energy density is given as

$$E_{hex} = K_0 + K_1(\alpha_1^2 + \alpha_2^2) + K_2(\alpha_1^2 + \alpha_2^2)^2 + K_3(\alpha_1^2 + \alpha_2^2)^3 + .. \quad (2.1)$$

where K's are the anisotropy constant, the energy is dependent only on α, the angle between magnetic field(H) and easy axis, K $\sin^2\alpha$ is minimum when α=0 for K > 0 . The shape anisotropy is only due to the shape of the material as the magnetization is affected by the macroscopic shape of the solid which in case of SW model is an ellipsoid with a uniaxial symmetry.

Hysteresis loop

A hysteresis loop is a characteristic curve that shows the variation in magnetization M with the applied field H. There is a propagation delay in M proportional to the width of hysteresis loop. At lower values of H, M varies proportionally with it. After certain value of H the materials attains a saturation magnetization M_s. At M_s all the magnetic moment are aligned in the direction of magnetic field,H. Multiple domain behaves like single domain. On reversing the H, M does not follow the same path. And at H=0, M$\neq$0 but instead shows a remnant magnetization M_r. To make M=0 a negative field

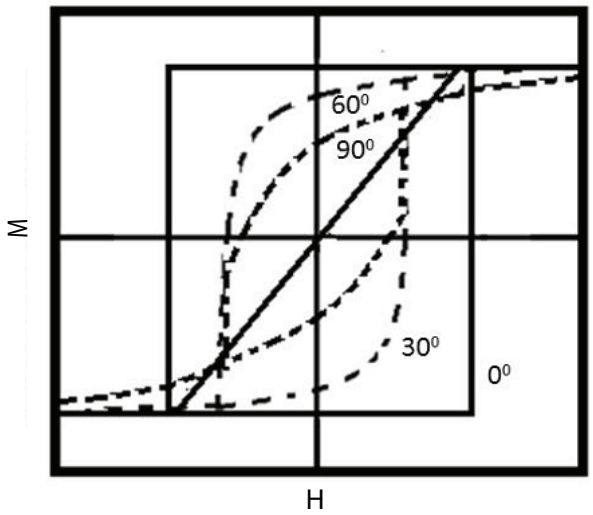

Figure 2.6: Hysteresis loop for the various angle of ϕ at 0^o, 30^o, 60^o and 90^o.

H_c is applied. H_c is defined as coercivity of the material. On continuing with reversal, saturation in negative quadrant is also observed. Again, reversing H, we get negative remnant magnetization and a positive coercivity of the material. It completes the full cycle of hysteresis loop[40].

In Fig. 2.6 different shapes of hysteresis curve is shown. The angle (sayϕ) between H and M alters the shape of the hysteresis curve. For $\phi = 0^o$ the loop is the broadest with a shape of a square. The ratio of $\frac{M_r}{M_s}$ of the loop is equal to 1. It defines the squareness of the loop. As ϕ increases the opening of the loop changes. When $\phi = 90^o$ the hysteresis loop reduces to a line that is H lies along the hard axis. The anisotropy field H_k can be obtained from the slope of M versus H curve(hysteresis loop)taken at ϕ=90^o. H_k is the field for which the magnetization is anisotropic before it reaches saturation. For a SW model H_k is found to be equal to H_c at $\phi = 0^o$. The other factors that affect the characteristics of a hysteresis curve are temperature and frequency

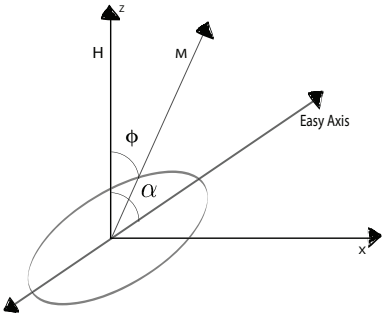

Figure 2.7: A single domain uniform magnetization in a shape of an ellipsoid in an external field H at an angle ϕ with easy axis.

of the applied field. The ferromagnet can loose all its properties above a certain temperature called Curie's temperature T_c. Above T_c, ferromagnets behave like a paramagnetic material.

2.4.2 Stoner-Wohlfarth model

Stoner-wohlfarth model of ferromagnetism is a simplest model that explains the physics of a fine magnetic grains in a single domain. Being single domain, domain related inhomogeneities are excluded and a uniform magnetization inside the domains is considered. In SW model the reversal of magnetization is considered to be under coherent rotation[41, 42]. The alignment of magnetic moment of a material material with uniform magnetization in 2D XZ plane ought to have an ellipsoid form[43, 44]. When an external field H is applied at an angle α with the anisotropy axis(easy axis) magnetization M moves in a two dimensional space given by angle ϕ with respect to H as shown in Fig. 2.7. For such a system the total energy density is a sum of the zeeman energy and the anisotropy energy. Also the alignment of magnetic moment is driven by the forces of anisotropy and the external field that

produces the total energy of the system.

$$\begin{aligned} E_{Total} &= E_{Ani} + E_{Zee} \\ E_{Ani} &= K_{eff} \sin^2(\alpha - \phi) \\ E_{Zee} &= M.H \\ E_{Total} &= K_{eff} \sin^2(\alpha - \phi) - HM_s \cos\phi \end{aligned} \tag{2.2}$$

K_{eff} is the anisotropy constant. The magnetic moment will align in the direction where the total energy of the system is minimized.But at some applied field magnetization shows discontinuity implying the process of switching(sudden change) while rotation. The effective anisotropy K_{eff} results from magneto crystalline anisotropy and shape anisotropy. The magneto crystalline anisotropy arises from the magnetization favouring towards a particular direction and shape anisotropy from the dependence of demagnetization on the geometry of the material[7, 36, 45].

$$K_{eff} = [K + 2\pi M_s^2(N_\perp - N_\parallel)] \sin^2(\alpha - \phi) \tag{2.3}$$

At equilibrium, the magnetization points along a direction defined by an angle ϕ^*, that minimizes the energy. The minimum energy at ϕ^* is given by

$$\left(\frac{\partial E}{\partial \phi}\right)_{\phi=\phi^*} = 0 \tag{2.4}$$

$$\left(\frac{\partial^2 E}{\partial \phi^2}\right)_{\phi=\phi^*} > 0 \tag{2.5}$$

Normalizing the magnetization by its saturation value, such that m = M/Ms,

gives

$$[\sin(\alpha)\cos(\alpha) + h\sin(\phi)]_{\phi=\phi^*} = 0, [\cos(2\alpha) + h\cos(\phi)]_{\phi=\phi} \geq 0 \qquad (2.6)$$

Two types of hysteresis curves can be considered the longitudinal hysteresis curve or the projection of M along H, $m_{\parallel}$ is given by cosϕ. And the transverse hysteresis curve or the projection of M perpendicularly to H,$m_{\perp}$ is given by sinϕ. The longitudinal hysteresis loop is used commonly. The energy equation 2.4 can be simplified and rewritten as a function of ϕ. It gives the change in energy of the magnetic moment.

$$E = \sin^2(\alpha - \phi) - h\cos\phi \qquad (2.7)$$

where

$$h = \frac{H}{H_k}$$

and the anisotropy field H_k is measured at the slope break of the hysteresis curve when H is along hard axis.

$$H_k = \frac{2K_{eff}}{\mu_0 M_s}$$

The stoner-wohlfarth numerical simulation is implemented to study the hysteresis loop and anisotropy of single magnetic domain of the samples at room temperature obtained from the magnetometry studies. In the model the hysteresis is plotted as a function of cosϕ with H[46].

Part II

Chapter 3

Materials and Methods

3.1 Materials

The spinel oxide and topological insulator are the class of material on which a dopant added in a crystal matrix leads to novel phenomena. The alteration of the structural and magnetic properties due to the dopant is recorded by varying the concentrations of the dopant. The different spectroscopic techniques implemented for the characterization of the structural and magnetic properties on doping are given below.

Two samples CoV_2O_4 and Bi_2Se_3 were doped with different concentration of dopant impurity. The samples were obtained from Dr. Sandip Chatterjee, Department of Physics, Indian Institute of Technology (Banaras Hindu University), Varanasi 221005, India.

$Li_xCo_{1-x}V_2O_4$ is a doped spinel oxide where non-metal Li ion is doped in CoV_2O_4. It comprises of 4 samples where x varies from 0, 0.05, 0.1 and 0.2. They are as follows,

- CoV_2O_4
- $Li_{0.05}Co_{0.95}V_2O_4$
- $Li_{0.1}Co_{0.9}V_2O_4$
- $Li_{0.2}Co_{0.8}V_2O_4$

$Li_xCo_{1-x}V_2O_4$ were prepared by solid state reaction route. LiO, CoO and V_2O_3 were mixed in appropriate ratios and pressed into pellets. The prepared pellets were sealed in quartz tube under high vacuum and heat treated into furnace at 8000^oC for 60h[47]. The obtained pellets of $Li_xCo_{1-x}V_2O_4$ were then crushed into powder for performing various measurements.

$Bi_{2-x}Se_3Co_x$ is a doped topological insulator where Co ion is doped in Bi_2Se_3. It comprises of 3 samples by varying the dopant concentration x from 0, 0.05 to 0.06. They are as follows,

- Bi_2Se_3
- $Bi_{1.95}Se_3Co_{0.05}$
- $Bi_{1.94}Se_3Co_{0.06}$

$Bi_{2-x}Se_3Co_x$ were prepared by melting a stoichiometric mixture. The mixture of high-purity Bi and Se elements was sealed in evacuated quartz ampoules. The ampoule was heated up to 8500^oC for 12 h and was kept at that temperature for 1 h. Then, it was slowly cooled to 6200^o for 46h and quenched in cold water. The obtained crystals were cleaved along the plane with shiny flat surface [48]. The crystal pellets were crushed into powder which was then used for performing various experiments.

The prepared samples were characterized using spectroscopic techniques to investigate structural and magnetic properties. To understand the structural modification we have employed various spectroscopic techniques like X-ray diffraction (XRD), fourier transform infrared (FT-IR), Raman spectroscopy etc. To understand the magnetic properties we have used superconducting quantum interfering device (SQUID) and electron paramagnetic resonance (EPR). In this work we have used simple SW model to explain the changes in H_c, K_{eff} and Easyspin simulation to obtain the g-anisotropy and spin values arising because of variation in the dopant.

3.2 Structural measurements

The techniques utilized for the structural characterization are as follows:

3.2.1 X-ray diffraction (XRD)

A crystalline substance has a highly ordered arrangement of atoms in a 3 dimensional space that repeats itself and forms a crystal lattice. The basic arrangement repeating itself throughout the lattice is called a unit cell. X-ray diffraction helps determine the arrangement of the crystal lattice. Since every ordered material is made up of a unique arrangement it gives unique diffraction pattern. XRD technique is a tool that helps determine the crystalline structure of the compound. XRD is a rapid analytical technique used for phase identification of a crystalline material and can provide information on unit cell dimensions. The information of the crystal planes in XRD is obtained from reflection of the incident X-rays from crystal planes at certain

angles. The reflected X-rays from the crystal planes interfere with one another as they leave the crystal. Based on their phase difference the reflection rays may interfere constructively or destructively giving an X-ray diffraction pattern. XRD is based upon the principle of Bragg's law which gives the relation between the wavelength of the X-ray and the angle of reflection given as

$$n\lambda = 2d\sin\theta \tag{3.1}$$

where d is the distance between atomic layers in a crystal, and λ is the wavelength of the incident X-ray beam and n is an integer[49]. The samples were characterized using PANalytical XPert Powder X-Ray diffractometer. The X-ray source used was Cu-Kα radiation of wavelength 1.54$\dot{A}$. The data was recorded for the 2θ range varied from 5^o to 90^o at room temperature.

3.2.2 Raman Spectroscopy

Raman spectroscopy is a molecular spectroscopy which is observed as inelastically scattered light. It is a technique which allows for the interrogation and identification of vibrational states of molecules. On interaction of light with molecules a small fraction of light is scattered. The spectrum of scattered light comprise of both elastic scattering(same frequency as of incident) and inelastic scattering(frequency shifted from incident). Up shifted frequency in the spectrum corresponds to anti-stokes line and down shifted frequency corresponds to stokes line. The elastic scattering of light is seen as Rayleigh line. Raman is a non-resonant technique. The shift of stokes/antistokes from the Rayleigh line called as Raman shift is independent of the exciting frequency,

so it allows to probe vibrational mode without disturbing the configuration of the molecules. Usually intensity of stokes lines are higher than the anti-stokes line because of the fact that the distribution of particles are higher in ground state than in excited state at room temperature. For Raman spectroscopy the instrument employed is Renishaw inVia RM2000 spectrometer. The laser used was of wavelength 785nm of power 30mW exposed for 20s and focused with 50X objective on the sample. The scan range was taken from 100cm^{-1} to 1000cm^{-1}, 3 accumulation scans were recorded.

3.2.3 Fourier transform infrared spectroscopy (FT-IR)

Fourier Transform Infrared Spectroscopy (FT-IR) is a technique which is used to analyze the chemical composition of the samples. It employes a method for measuring all of the infrared frequencies simultaneously, rather than individually. The spectrometer has an interferometer which produces a signal which has all of the infrared frequencies encoded in it. All the datas are measured as an encoded signal which is decoded using the mathematical tool called the Fourier transformation which then gives the plot of intensity at each individual frequency[50]. This spectrum carries information that can be divided in two regions. The infrared region from 500cm^{-1} to 1500cm^{-1} is called the fingerprint region. It depends on complex vibrations involving the entire molecules. The region from 1500cm^{-1} to 4000cm^{-1} is called the functional group region. This region shows absorption arising from the stretching modes in the molecule[51]. The FT-IR spectrometer used for the analysis of the sample is Perkin Elmer spectrum 100 FT-IR Spectrometer. The scanning

range was taken from 700cm^{-1} to 4000^{-1}.

3.3 Magnetic Characterization

The dopant in the given samples not only influence the structural properties but affects the magnetic properties as well. The changes in the magnetic behaviour is studied using two techniques, SQUID and EPR.

3.3.1 Superconduction quantum interfering device (SQUID)

The superconducting quantum interference device (SQUID) consists of two superconductors separated by thin insulating layers to form two parallel Josephson junctions. The device may be configured as a magnetometer to detect small magnetic fields. The SQUID device is highly sensitive technique which can measure changes in magnetic field associated with one quantum of the magnetic flux.

The measurements were performed using Quantum design SQUID VMS instrument and MPMS3 Multi VU software. The temperature during the measurements were 80K and 300K. The scan range of magnetic field was -30000Oe to 30000Oe for $Li_xCo_{1-x}V_2O_4$ and -2000Oe to 2000Oe for $Bi_{2-x}Se_3Co_x$. A subtraction of diamagnetic contribution on hysteresis curves of $Li_xCo_{1-x}V_2O_4$ and $Bi_{2-x}Se_3Co_x$ is done to obtain purely ferromagnetic magnetic hysteresis curve.

3.3.2 Electron paramagnetic resonance (EPR)

Electron Spin Resonance is a technique that provides the electronic structure of organic, inorganic species which includes organic free radicals, biradicals, triplet excited state etc. It works due to the resonance of the magnetic field with the energy gap. The relationship between the energy difference ΔE and the absorption of electromagnetic radiation is given by ΔE=hυ. where h is Planck's constant and υ is the frequency of the radiation. The energy differences studied in EPR spectroscopy are predominately due to the interaction of unpaired electrons in the sample with a magnetic field. This effect is called the Zeeman Effect. It splits energy levels of an electron in presence of magnetic field. ForS=1/2 , spin quantum numbers m_s = -1/2,+1/2. The energy of each orientation is the product of magnetic moment μ and magnetic field B. For an electron $\mu = m_s g_e \beta$, where β the Bohr magneton and g_e is the spectroscopic g-factor of the free electron($g_e \approx 2$)[52, 53]. The energies of spin -1/2,+1/2 are

$$\begin{aligned} E_{1/2} &= 1/2 g_e \beta B \\ E_{-1/2} &= -1/2 g_e \beta B \end{aligned}$$

In EPR spectrometer, a paramagnetic sample is placed in a large uniform magnetic field which splits the energy levels of the ground state by an amount ΔE. A peak in the absorption occurs when the magnetic field tunes to the two spin states so that their energy difference matches the energy of the radiation. An EPR spectrum is usually acquired by varying the magnetic field while irradiating the sample with electromagnetic radiation at a fixed frequency,

and consists of absorption plotted against magnetic field. The Microwave radiation is applied perpendicular to the magnetic field and absorption takes place at resonance. The EPR experiments of the samples are performed using JES-FA series ESR spectrometers, the microwave frequency given was 9443.44MHz for $Li_xCo_{1-x}V_2O_4$ and 9288.032MHz for $Bi_{2-x}Se_3Co_x$ equipped with a modulation frequency, modulation amplitude and time constant as 100 KHz, 100mT and 0.03s respectively. The scan range was 86 mT -586 mT with 1 accumulation scan.

Part III

Results and Discussion

Chapter 4

Doping Li ion in CoV_2O_4

The CoV_2O_4 spinel oxide matrix is doped with Li with different concentration, $Li_xCo_{1-x}V_2O_4$ x=0, 0.05, 0.1 and 0.2. Li is an alkali metal it substitutes the transition metal ion Co in the tetrahedral A site of the spinel formula AB_2O_4 while the octahedral B site remains undisturbed. This influences the atomic interaction resulting in modification of molecular vibrations, bond lengths, magnetic interactions etc. In this chapter we present the structural and magnetic characterizations of $Li_xCo_{1-x}V_2O_4$. The investigation on crystallographic symmetries and vibrational modes related to the chemical bonds of the undoped CoV_2O_4 and doped $Li_xCo_{1-x}V_2O_4$ is discussed in the structural characterization utilizing X-ray diffraction, Raman and FT-IR spectral analysis. The magnetic interactions will also be discussed using SQUID, SW model and EPR analysis .

4.1 Structural characterization

4.1.1 X-ray diffraction

The X-ray diffraction pattern of CoV_2O_4 is shown in Fig. 4.1(1). The pattern shows that all peaks are in good agreement with the face centered cubic nature of JCPDS file no. 73-1633 of Co_2VO_4 and 82-2395 of $LiCoVO_4$. No secondary phase or impurity peaks were observed. The obtained diffraction peaks suggest that CoV_2O_4 is well crystallized[54]. The maximum intensity peak appears at 35.5^o which corresponds to (311) plane. The peaks appearing at 30.11^o, 43.10^o, 53.47^o, 56.97^o, 62.56^o, 73.97^o, 89.55^o, 78.86^o corresponds to (220),(400),(422), (511), (440), (533) and (642) planes respectively[55]. The obtained $2\theta^o$ and corresponding peaks along with the calculated lattice parameter a are given in Table 4.1. The lattice parameters are calculated using the formula

$$\frac{a^2}{h^2+k^2+l^2} = \frac{\lambda^2}{4\sin^2\theta}$$

where λ is the wavelength of incident Cu X-ray radiation which is 1.54 $\dot{A}$ and *(hkl)* are the Miller indices of the crystal plane.

Fig. 4.1(2) show the XRD patterns of $Li_xCo_{1-x}V_2O_4$ where x= 0, 0.05, 0.1 and 0.2. The XRD patterns of $Li_xCo_{1-x}V_2O_4$ is similar to undoped CoV_2O_4 where peaks appear at similar 2θ values. From Fig.4.1(2) it can be seen that no new peaks arise on the incarceration of dopant Li. The crystallinity of the sample remains undisturbed with the insertion of Li in CoV_2O_4. On careful observation the XRD peak corresponding (311) plane shifts to-

wards the higher θ^o values as the concentration of Li changes from 0 to 0.2 in $Li_xCo_{1-x}V_2O_4$. It is an evidence that the lattice parameter is reduced upon doping as shown in Table 4.2. The crystal system upon doping Li ion does not change. Thus the samples crystalize in face centered cubic system of Fd3m space group. Fig. 4.2 is the plot of lattice parameter, a versus the dopant concentration x in $Li_xCo_{1-x}V_2O_4$. The lattice parameter decreases linearly with increasing Li concentration in $Li_xCo_{1-x}V_2O_4$. CoV_2O_4 is distorted to smaller spacing when Li gets incorporated into the crystal lattice[56]. The lattice parameter versus the concentration plot was fitted using linear fit of a=mx+C, where a is the lattice parameter in Angstrom($\dot{A}$), x is the concentration of Li, m is the slope and C the intercept of the fit. The slope m gives the rate of decrease of the lattice parameter when x changes from 0 to 0.2 whereas intercept C provides the value of lattice parameter when the crystal is undoped. From the fit value of m was found to be -0.149($\pm$0.017)and C was found to be 8.340($\pm$0.002).

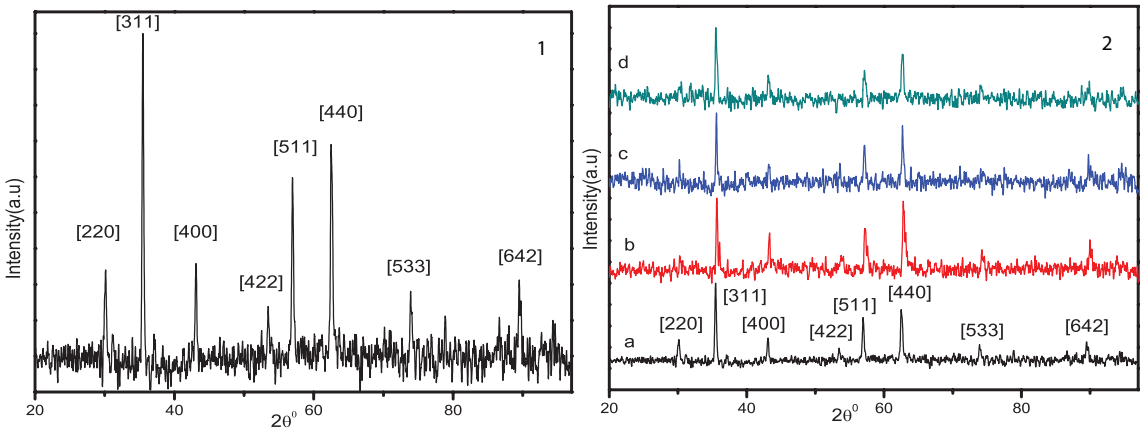

Figure 4.1: XRD pattern of (1)CoV_2O_4 and (2)(a)CoV_2O_4 , (b)$Li_{0.05}Co_{0.95}V_2O_4$, (c)$Li_{0.1}Co_{0.9}V_2O_4$, (d)$Li_{0.2}Co_{0.8}V_2O_4$.

Table 4.1: The obtained peak position in $2\theta^o$, peak intensity, calculated lattice parameter a and Miller indices *(hkl)* of $Li_xCo_{1-x}V_2O_4$ where x=0,0.05,0.1 and 0.2.

CoV_2O_4		$Li_{0.05}Co_{0.95}V_2O_4$		$Li_{0.1}Co_{0.9}V_2O_4$		$Li_{0.2}Co_{0.8}V_2O_4$		
$2\theta^o$	a	$2\theta^o$	as	$2\theta^o$	a	$2\theta^o$	a	*(hkl)*
	$(\dot{A})$		$(\dot{A})$		$(\dot{A})$		$(\dot{A})$	
30.11	8.382	30.31	8.327	30.20	8.351	30.29	8.33	220
35.49	8.376	35.54	8.364	35.57	8.36	35.63	8.345	311
43.10	8.381	43.31	8.344	43.26	9.04	43.20	8.36	400
53.47	8.382	53.83	8.329	53.57	9.34	53.76	8.339	422
56.97	8.386	57.26	8.347	57.16	16.75	57.19	8.36	511
62.56	8.387	62.89	8.346	62.72	8.37	62.69	8.37	400
73.97	8.390	74.35	8.353	73.96	8.391	74.15	8.372	533
89.55	8.179	90.04	8.143	89.76	8.164	89.78	8.162	642

The lattice parameter directly depends on the ionic size of the atoms present in the crystal. Ionic size of Li is $0.73\dot{A}$ and of Co is $0.72\dot{A}$. It can be noted that the two ionic sizes are comparable thus the size of the dopant cannot contribute to the decrease in lattice parameter. Li has no 2p or 3d electrons in its outer atomic shell while Co has 7 3d electrons in valence shell, Thus the weak coulomb interaction due to the dopant may reduce the lattice parameter[6].

The effectiveness of scattering X-rays is called the scattering factor,f it depends on the Bragg's angle. The structure factor ($F_{(hkl)}$) represents the resultant amplitude and phase of scattering of all the electron density distribution of one unit cell. The structure factor depends on position of each atom and its scattering factor which is directly proportional to intensity of

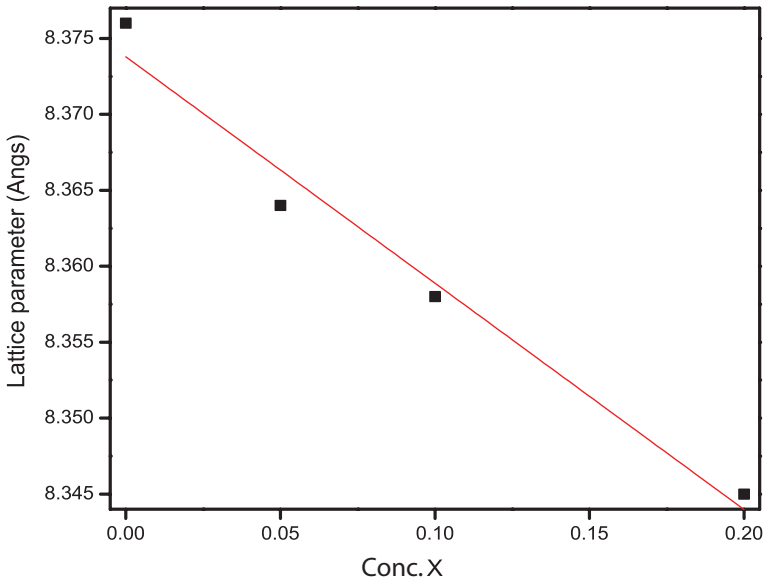

Figure 4.2: Lattice parameter, a versus the dopant concentration x of $Li_xCo_{1-x}V_2O_4$ where x changes from 0 to 0.2.

reflection[57]

$$F_{(hkl)} = 2\sum f \cos 2\pi(hx + ky + lz)$$
$$F^2_{(hkl)} = I_{(hkl)}$$

where x, y and z are the fractional cordinates, *(hkl)* are Miller indices and $I_{(hkl)}$ is the intensity of reflection from *(hkl)* plane. Fig. 4.3 is peak intensity of (311) plane versus the concentration x. The peak intensity decreases with increasing Li concentration in $Li_xCo_{1-x}V_2O_4$. The decrease in intensity upon doping attributes to a change in electron density causing a destructive interference of the reflected X-rays.

Using XRD we have successfully identified the nature of the crystal structure. The influence of dopant Li ion in $Li_xCo_{1-x}V_2O_4$ for the given concentra-

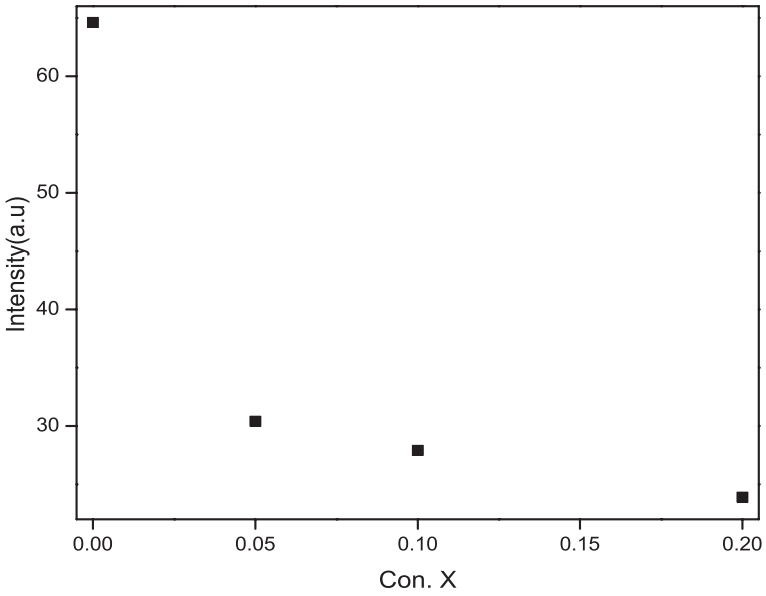

Figure 4.3: Peak intensity of (311) plane versus the dopant concentration x of $Li_xCo_{1-x}V_2O_4$ where x changes from 0 to 0.2.

Table 4.2: Lattice parameter and peak intensity of (311) plane of $Li_xCo_{1-x}V_2O_4$ where x=0,0.05,0.1 and 0.2.

sample	Lattice parameter ($\dot{A}$)	peak Intensity (a.u)
CoV_2O_4	8.376	64.61
$Li_{0.05}Co_{0.95}V_2O_4$	8.364	30.40
$Li_{0.1}Co_{0.9}V_2O_4$	8.358	27.90
$Li_{0.2}Co_{0.8}V_2O_4$	8.345	23.9

tion is also interpreted in terms of lattice parameter and peak intensity. The change in lattice parameters and bond lengths can be further investigated using FT-IR and Raman spectral analysis.

4.1.2 FT-IR and Raman spectral analysis

The IR spectra of CoV_2O_4 is shown in Fig. 4.4(1). The sharp peaks between 1000 to 1100cm^{-1} shows the absorption spectrum of V_2O_4. It corresponds to the Vanadyl stretching of V=O[58]. Also the band at 878cm^{-1} is due to the vibration of V-O-V bridges. The peaks in the range 2800-3600cm^{-1} show the OH absorption peaks[59, 60, 61]. The FT-IR spectra of $Li_xCo_{1-x}V_2O_4$ are shown in Fig. 4.4(2). The FT-IR spectra show negligible changes upon doping of Li. While doping Li in CoV_2O_4 the concentration of Co also changes. Pertaining to the change in its concentration, the vibrations associated with Co ion should be seen below 1000cm^{-1}. The IR spectra below 1000cm^{-1} are similar in nature therefore could not be distinguished with the change in concentration of Li ion. Due to the instrumental constraints the FT-IR measurements could not be performed below 600cm^{-1}, this is why in order to elucidate the changes in Co ion vibrations Raman spectroscopy is performed.

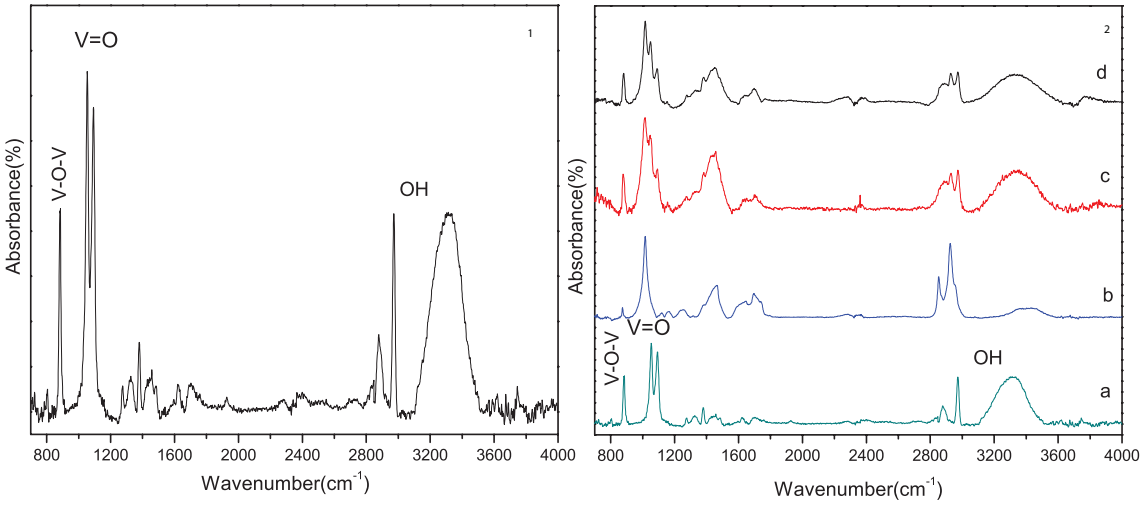

Figure 4.4: FT-IR spectra of (1)CoV_2O_4 and (2)(a)CoV_2O_4, (b)$Li_{0.05}Co_{0.95}V_2O_4$, (c)$Li_{0.1}Co_{0.9}V_2O_4$ and (d)$Li_{0.2}Co_{0.8}V_2O_4$

The Raman spectra of CoV_2O_4 is shown in Fig. 4.5(1). The obtained Raman position and strength are tabulated in Table 4.3. Raman spectroscopy is sensitive to metal(M)-oxygen(O)vibrations. The metal-oxygen vibrations usually lie in the 100-1200 cm^{-1} region. Raman spectrum of CoV_2O_4 displays number of peaks ranging from 700 to 960cm^{-1} which corresponds to the vanadate species of the sample[62]. In the octahedrally coordinated vanadate sample a sharp peak at 842cm^{-1} followed by weak intensity peaks in between 840^{-1} to 960cm^{-1} are observed which corresponds to the terminal V=O stretch. The presence of very weak intensity peak at 467cm^{-1} corresponds to ν_{O-Co-O} E_{2g} bending mode, while the peaks at 550cm^{-1} and 595cm^{-1} are assigned to ν_{Co-O} A_{1g} stretching vibrations[63, 64]. The broad band at 834cm^{-1} is attributed to the V-O-V stretches in two-dimensional distorted polyvanadates[62, 65, 66]. The Raman peaks of metal oxygen are rather weak in the two major regions at 400-550cm^{-1} and 550-750 cm^{-1} and can nevertheless be distinguished. They correspond to spectral domains where the skeletal vibrations, the deformation modes of the Cobalt-oxygen chain of Co-O occurs. The peaks below 400cm^{-1} can be assigned to different O-V-O vibrations[67].

Raman spectra of $Li_xCo_{1-x}V_2O_4$ are shown in Fig. 4.5(2). The obtained Raman peaks and their strength of $Li_xCo_{1-x}V_2O_4$ are given in Table 4.3. The Raman peaks of Li doped $Li_xCo_{1-x}V_2O_4$ are similar to that of undoped CoV_2O_4. The only observable changes are seen in the peaks intensities of the Raman spectra. Upon doping Li ion in $Li_xCo_{1-x}V_2O_4$ no significant change in metal-oxygen Co-O peaks are observed, whereas the peak intensity corresponding to V-O-V reduces significantly.

Table 4.3: Raman peaks and the peak intensities of $Li_xCo_{1-x}V_2O_4$ for x= 0,0.05,0.1 and 0.2. The assigned peaks are labelled corresponding to their interactions.

CoV_2O_4		$Li_{0.05}Co_{0.95}V_2O_4$		$Li_{0.1}Co_{0.9}V_2O_4$		$Li_{0.2}Co_{0.8}V_2O_4$		
position	strength	position	strength	position	strength	position	strength	Assigned
(cm^{-1})	(a.u)	(cm^{-1})	(a.u)	(cm^{-1})	(a.u)	(cm^{-1})	(a.u)	peaks
115.33	0.12(w)	115.27	0.05(v.w)	115.79	0.07(w)	114.21	0.08(w)	
139.40	0.25	141.09(w)	0.06	142.30	0.05(v.w)	141.21	0.07(w)	V-O-V[27]
162.90	0.06(w)	162.68	0.04(v.w)	164.42	0.04(v.w)	162.28	0.05(v.w)	V-O-V
191.85	0.04(v.w)	190.06	0.03(v.w)	201.57	0.01(v.w)	195.87	0.03(v.w)	V-O-V
287.87	0.10(w)	270.11	0.04(v.w)	269.48	0.04(v.w)	270.60	0.06(w)	O-V-O
330.10	0.03(v.w)	299.54	0.04(v.w)	298.70	0.06(w)	296.32	0.07(w)	O-V-O
		327.49	0.03(v.w)	329.13	0.03(v.w)	323.01	0.06(w)	O-V-O
392.18	0.08(w)	392.52	0.03(v.w)	392.06	0.04(v.w)	389.71	0.05(v.w)	O-V-O[62]
550.45	0.02(v.w)	552.73	0.01(v.w)	554.40	0.01(v.w)	549.10	0.02(v.w)	O-Co-O[24]
595.48	0.03(v.w)	593.06	0.02(v.w)	593.63	0.02(v.w)	591.34	0.03(v.w)	Co-O[65]
834.48	0.24(s)	832.30	0.35(v.s)	831.47	0.31(v.s)	831.50	0.37(v.s)	V-O-V
842.49	0.52(v.s)	842.40	0.33 (v.s)	842.98	0.46(v.s)	841.78	0.42(v.s)	V=O[61]
903.39	0.08(v.s)	901.75	0.10 (w)	90 .72	0.10(w)	900.76	0.11(w)	V=O
937.86	0.08(w)			936.99	0.06(w)			V=O

[1]here v.w, w, s,s.w represents very weak, weak, strong and very strong peaks respectively

A change in lattice parameter a occurs in $Li_xCo_{1-x}V_2O_4$ matrix upon doping. A change in Raman vibrational frequencies and peak intensities are observed as the insertion of Li ion affects the local environment of $Li_xCo_{1-x}V_2O_4$. The interaction of Li ion in crystal matrix are further investigated in magnetic characterization of $Li_xCo_{1-x}V_2O_4$.

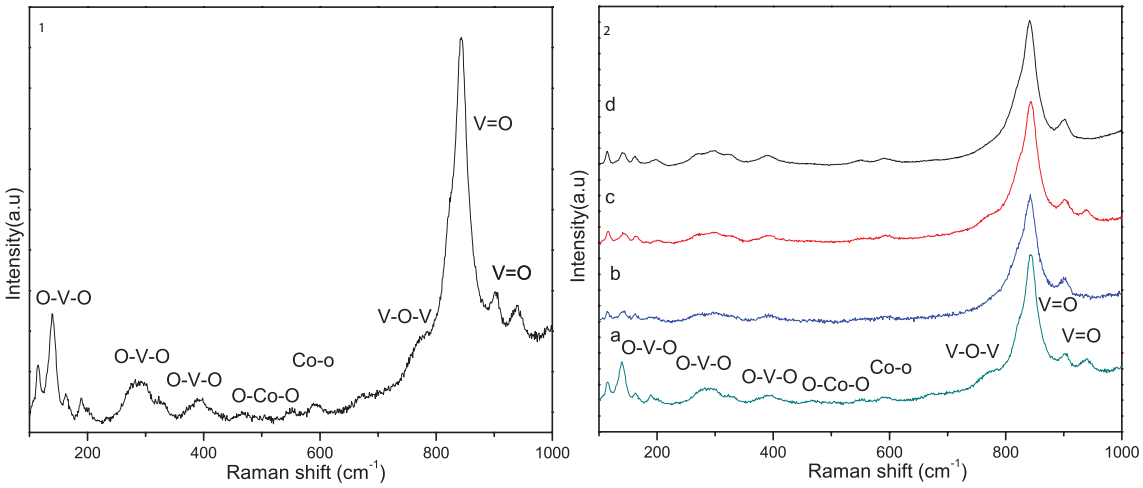

Figure 4.5: Raman spectra of (1)CoV_2O_4 and (2)(a)CoV_2O_4, (b)$Li_{0.05}Co_{0.95}V_2O_4$, (c)$Li_{0.1}Co_{0.9}V_2O_4$ and (d)$Li_{0.2}Co_{0.8}V_2O_4$.

4.2 Magnetic characterization

The magnetic behaviour such as diamagnetism, paramagnetism and ferromagnetism of CoV_2O_4 and $Li_xCo_{1-x}V_2O_4$ will be examined in this section. The change in the properties is characterized with the help of SQUID and EPR at 300K and 80K. The Stoner-Wholfarth model is used to study the magnetic hysteresis of $Li_xCo_{1-x}V_2O_4$ at 300K.

4.2.1 EPR spectroscopy

Electron paramagnetic resonance has been used to study the effects of Li doping in $Li_xCo_{1-x}V_2O_4$ spinel oxide. Electron paramagnetic resonance occurs when an unpaired electrons interacts with the magnetic field giving rise to a zeeman splitting of the spin state. The total hamiltonian of the system is

given as a sum of diamagnetic, paramagnetic and ferromagnetic energy[7, 50].

$$H = H_{Dia} + H_{Zee} + H_{Exc}$$

Fig. 4.6(a) is the EPR spectrum of CoV_2O_4 at 300K where the field is scanned between of 86 mT to 586 mT. The spectrum is also been simulated using an easyspin software and the simulated spectrum is also shown in the same figure. The parameters like spin integral, g value and linewidth were simulated in order to get the best fit possible. The obtained parameters are also tabulated in Table 4.4. In Fig. 4.6(a) an EPR peak at an isotropic g value equals to 2.15 for S=1/2 is observed which confirms the presence of paramagnetic interaction in CoV_2O_4. The g value of a free electron is $g_e \simeq 2$, in CoV_2O_4 the obtained $g > g_e$. It suggests the electron is not completely free, rather its trapped in the crystal matrix. The linewidth of the observed EPR signal is found to be 140mT. This broad linewidth also reveals that the electron in the matrix is interacting with its local environment giving rise to an inhomogeneous broadening in the EPR signal.

The linewidth is inversely proportional to the lifetime of spin in the excited state.

$$\triangle E . \triangle t \geq \hbar$$

From the Heisenberg uncertainty principle the above equation holds good. In the above relation $\triangle$ E = g$\beta\triangle$B where $\triangle$B is the linewidth in Tesla and $\triangle$t is the lifetime of the excited state. From the EPR spectrum of CoV_2O_4 at 300K the lifetime of excited state is found to be 3.8×10^{-11}s. EPR not only deals with the electronic structure of paramagnetic centres, but also

with their local environments[68]. At low temperatures and in most of the environments, the dipole-dipole interaction and exchange interaction mask the paramagnetic effects of neighbouring spins. The could be the reason that at low temperatures(80K) we have not observed any EPR signal in CoV_2O_4.

In Fig. 4.6 the room temperature EPR spectra of $Li_xCo_{1-x}V_2O_4$ are also shown. The corresponding simulated spectra are also plotted in the respective figures. The simulated parameters are tabulated in Table 4.4. It can be seen that upon doping Li in $Li_xCo_{1-x}V_2O_4$ a uniaxial anisotropy g is added along with isotropic g anisotropy of undoped CoV_2O_4. It reveals that an addition of Li in CoV_2O_4 introduces uniaxial anisotropy in the spin environments. The g values for the doped system has two different g values where g_{xx}=g_{yy}≠g_{zz}. This uniaxial anisotropy could be due to the inhomogeneity in the crystal environment and the spin system. The uniaxial anisotropy persists in $Li_xCo_{1-x}V_2O_4$ upto x=0.1. For dopant concentration x=0.2 in $Li_xCo_{1-x}V_2O_4$ the uniaxial anisotropy vanishes and the crystal system behaves like an isotropic spin medium. It means this can be attributed to heavily doped CoV_2O_4 with Li ion, with it increases the electron density in the crystal matrix uniformly. Like CoV_2O_4 no EPR spectra is observed for $Li_xCo_{1-x}V_2O_4$ at 80K this means other interactions like dipole-dipole interaction and exchange interaction may mask the paramagnetic effect in these crystals.

The obtained lifetime of the upper state for all the observed spin is found to be of the order of 10^{-11}s this is why these materials may not find potential application in magnetic storage devices at room temperature.

The magnetic behaviour of $Li_xCo_{1-x}V_2O_4$ at 300K and 80K can be in-

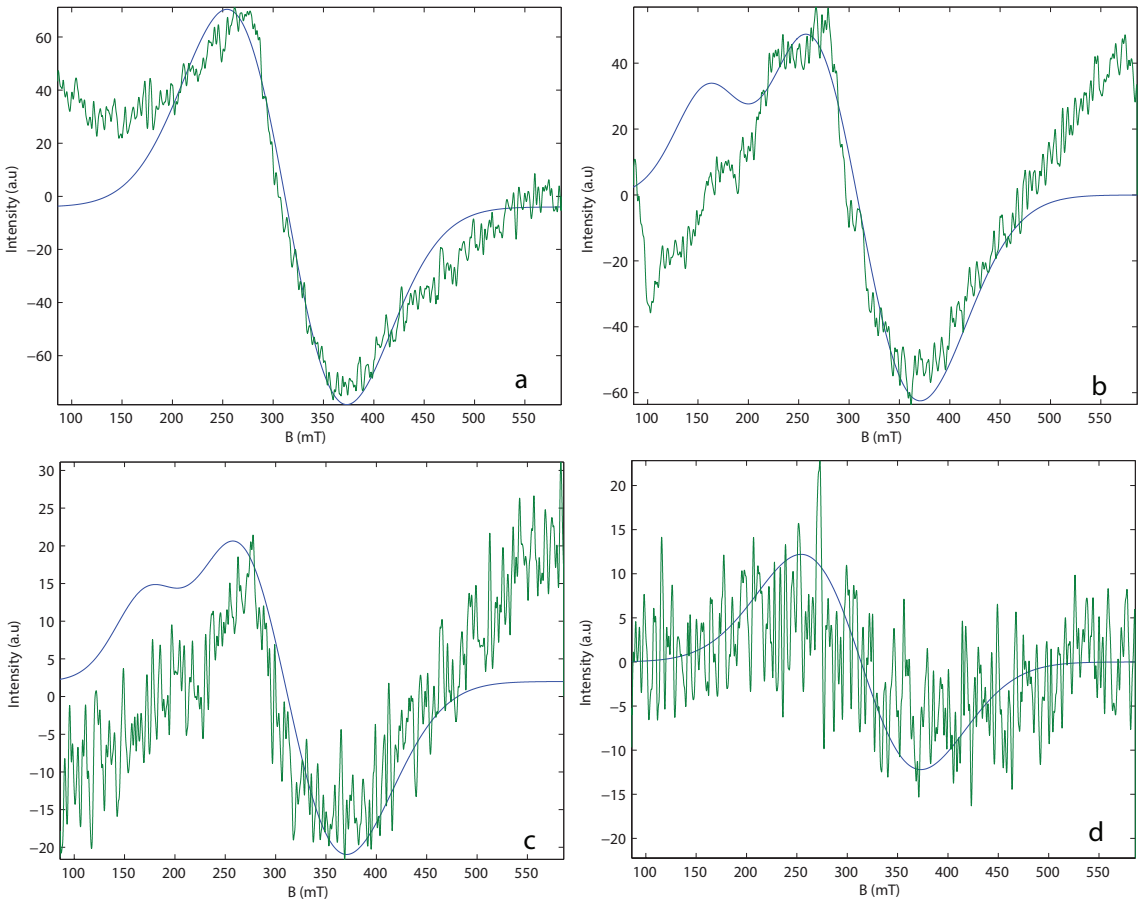

Figure 4.6: EPR spectra of experimental(green line) and simulated(blue line) (a)CoV_2O_4, (b)$Li_{0.05}Co_{0.95}V_2O_4$, (c)$Li_{0.1}Co_{0.9}V_2O_4$ and (d)$Li_{0.2}Co_{0.8}V_2O_4$ at 300K.

vestigated in terms of magnetic hysteresis curves. The anisotropy present in $Li_xCo_{1-x}V_2O_4$ matrix can also be supported with SW mathematical model and SQUID magnetometry.

Table 4.4: Obtained g value, spin integral, linewidth and lifetime of $Li_xCo_{1-x}V_2O_4$ where x=0,0.05,0.1 and 0.2.

sample	spin	g value			Linewidth	Lifetime
		g_{xx}	g_{yy}	g_{zz}	mT	10^{-11} s
CoV_2O_4	1/2	2.15	2.15	2.15	140	3.8
$Li_{0.05}Co_{0.95}V_2O_4$	1/2	2.15	2.15	2.15	140	3.8
	1/2	3.9	3.9	2.18	80	4.3
$Li_{0.1}Co_{0.9}V_2O_4$	1/2	2.15	2.15	2.15	140	3.8
	1/2	3.7	3.7	2.12	75	4.8
$Li_{0.2}Co_{0.8}V_2O_4$	1/2	2.15	2.15	2.15	140	3.8

4.2.2 SQUID magnetometry

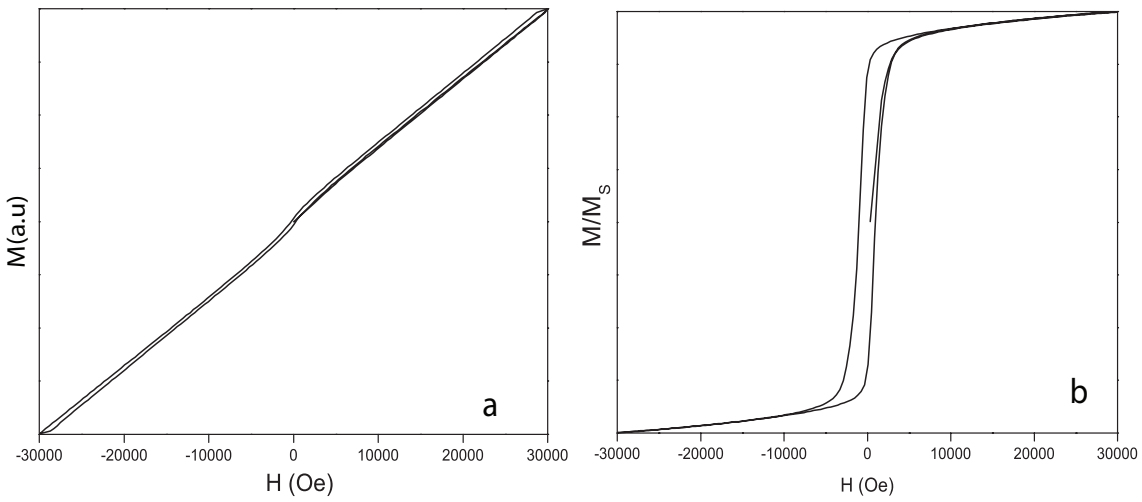

Figure 4.7: The hysteresis curve of (a)CoV_2O_4 at 300K and (b)CoV_2O_4 at 80K

The hysteresis curve of CoV_2O_4 at 300K is shown in Fig. 4.7(a). The hysteresis curve was obtained while varying the applied magnetic field, H between +30000Oe to -30000Oe and monitoring the changes in the magnetization ,M. In the applied magnetic field range at 300K no saturation of magnetization M_s is observed. The coercivity, H_c and remnant magnetization, M_r of CoV_2O_4 are found to be 295.8 Oe and 1.7×10^{-2} emu g^{-1} respectively.

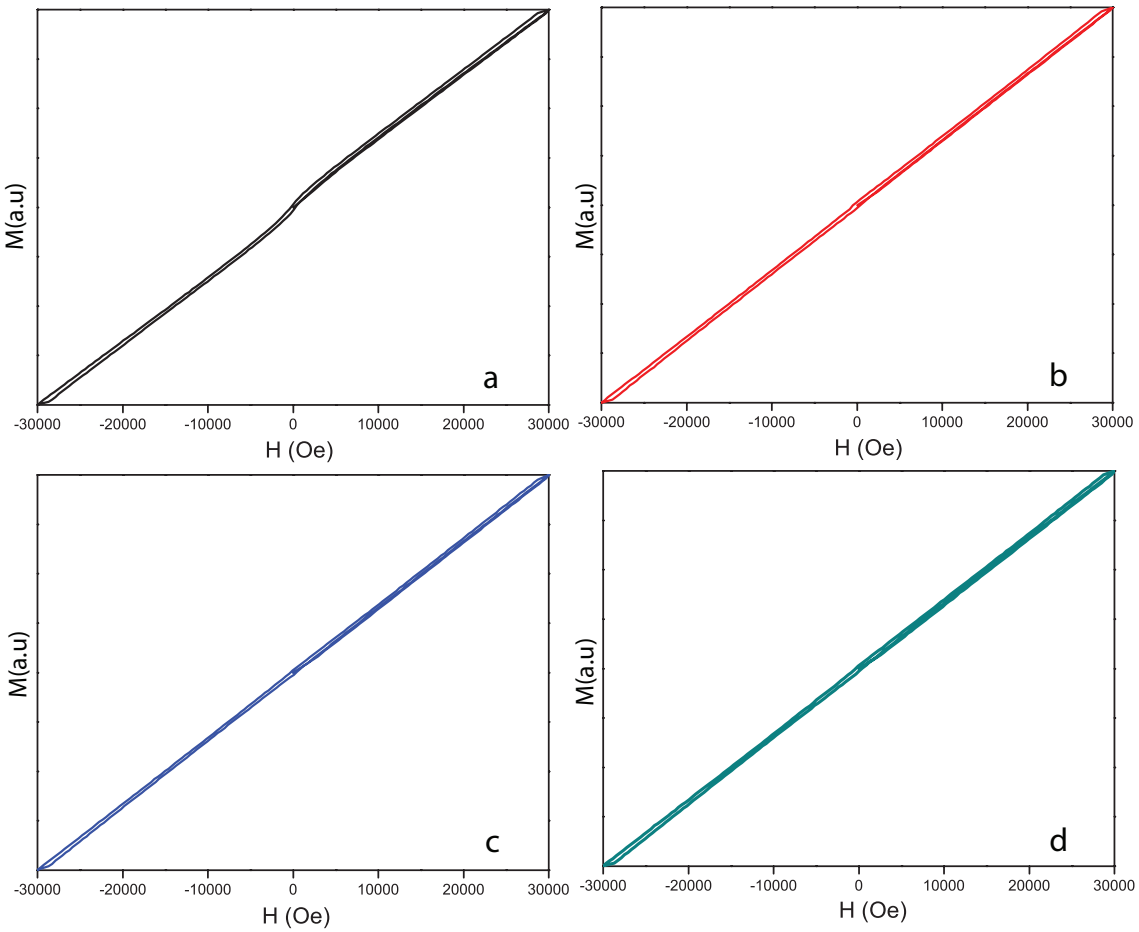

Figure 4.8: The hysteresis curve of (a)CoV_2O_4 , (b)$Li_{0.05}Co_{0.95}V_2O_4$, (c)$Li_{0.1}Co_{0.9}V_2O_4$, (d)$Li_{0.2}Co_{0.8}V_2O_4$ at 300K.

In Fig. 4.7(b) a the hysteresis curve of CoV_2O_4 at 80K is shown. Here also H varies from +30000 Oe to -30000 Oe. The obtained saturation magnetization M_s is 33.77emu g^{-1}, Coercivity, H_c is found to be 1017.25 Oe and remnant magnetization, M_r is 23.75emu g^{-1}. The presence of H_c and M_r in CoV_2O_4 at both temperatures i.e at 300K and 80K show that this material is ferromagnetic. The increase in H_c and M_r at lower temperature reveals an increased exchange interaction in CoV_2O_4.

The room temperature hysteresis curves of $Li_xCo_{1-x}V_2O_4$ are shown in

Fig. 4.8(b,c,d). H ranges between -30000 Oe and -30000Oe. No M_s is observed in the range of applied H. The obtained value of H_c and M_r given in Table 4.5. It can be seen the coercivity of the samples at 300K increases while increasing Li concentration from 0.05 to 0.2 in $Li_xCo_{1-x}V_2O_4$. It can be seen from the table that at 300K the H_c and M_r are small and similar to that of CoV_2O_4, it can be attributed to weak ferromagnetic effects of these samples at 300K.

Fig. 4.9 shows the hysteresis curve of $Li_xCo_{1-x}V_2O_4$ at 80K. It can be seen from the figures that saturation magnetization,M_s is attained for $Li_xCo_{1-x}V_2O_4$ where x goes from 0 to 0.2. The values of H_c and M_r as observed from the hysteresis curves of $Li_xCo_{1-x}V_2O_4$ at 80K are also tabulated in Table 4.5. The low temperature H_c and M_r are larger as compared to those obtained at 300K. This can be attributed to enhanced exchange interaction in $Li_xCo_{1-x}V_2O_4$ at low temperatures. From the table it can be easily noted that H_c and M_r reduces with increase in Li concentration in $Li_xCo_{1-x}V_2O_4$. The small coercivity in a material is an indication of easily favourable domain walls movement upon minutely changing magnetic field. Such behaviour is seen in soft magnetic materials. It means doping Li in $Li_xCo_{1-x}V_2O_4$ turns it in a more softer magnetic material than CoV_2O_4 .

From the EPR analysis it has been observed that $Li_xCo_{1-x}V_2O_4$ posses a uniaxial anisotropy. A simple Stoner-Wohlfarth model valid for a single magnetic domain with uniaxial anisotropy is used to simulate the room temperature hysteresis curve. The total energy density of a single magnetic grain

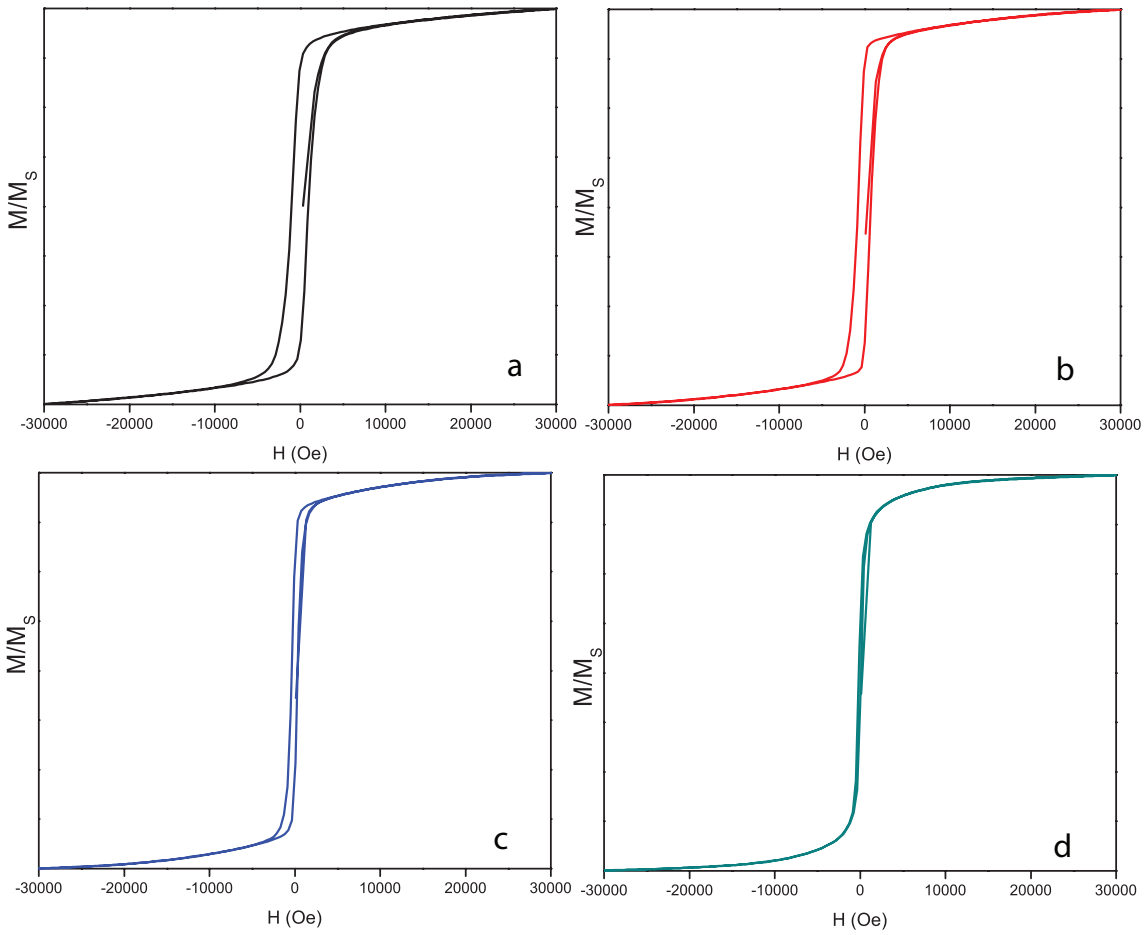

Figure 4.9: The hysteresis curve of(a)CoV_2O_4 , (b)$Li_{0.05}Co_{0.95}V_2O_4$, (c)$Li_{0.1}Co_{0.9}V_2O_4$, (d)$Li_{0.2}Co_{0.8}V_2O_4$ at 80K.

$$E_{Total} = K_{eff} \sin^2(\alpha - \phi) - HM_s \cos\phi$$

It is the sum of the anisotropy energy and the zeeman energy. Here ϕ is the angle between the magnetization M and applied field H and α is the angle

between H and easy axis. Energy as a function of ϕ is given as

$$E(\phi) = \sin^2(\alpha - \phi) - h\cos\phi$$

Where h=H/H_k and anisotropy field $H_k = 2K_{eff}/M_s$. Effective anisotropy energy density K_{eff} can be calculated by the relation

$$K_{eff} = \frac{M_s}{2} H_k$$

Fig. 4.10 shows the experimental and simulated hysteresis curves of the $Li_xCo_{1-x}V_2O_4$ at 300K. It can be noted that from above equation energy density is a function of ϕ. The simulated hysteresis loop is plotted H versus cosϕ where ϕ is the value obtained during the energy minimization. The aim of the simulation is to recreate the experimental hysteresis curve and to find the important parameters on which the coercivity H_c, remnant magnetization M_r etc. depends. The simulation require two initial fitting parameter H_k and α. Where α is the angle between H and the easy axis of the material and H_k is the anisotropy field. In Fig. 4.10 the simulated hysteresis curves for $Li_xCo_{1-x}V_2O_4$ are also shown. For simulation the value of α used is 89.5^o and H_k is 11.54×10^5. The simulated parameters such as H_k, M_s etc. are given in Table 4.6.

The alignment of magnetic moments of a material is easier in some direction and harder in other. The axis on which the alignment is easily favourable is easy axis and where it is difficult is called hard axis. The angle between the easy axis and the hard axis of any material is 90^o, also from the simulation

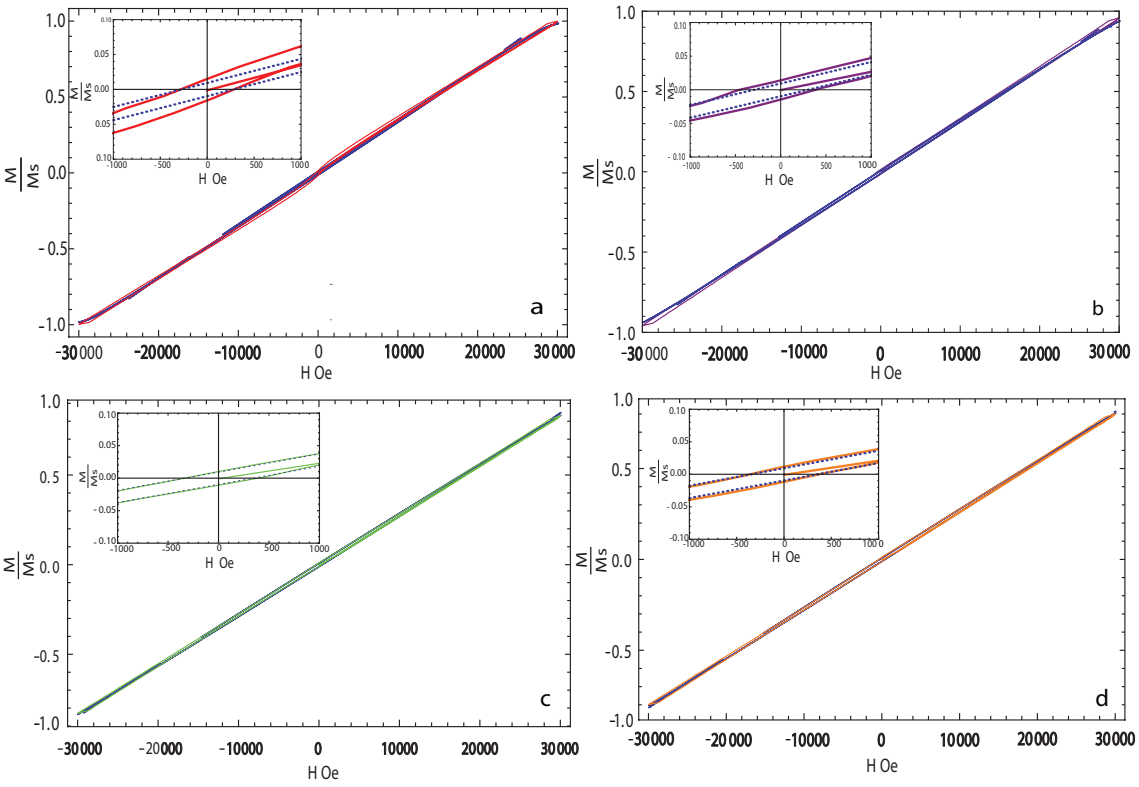

Figure 4.10: Simulated curve(blue line) of (a)CoV_2O_4 , (b)$Li_{0.05}Co_{0.95}V_2O_4$, (c)$Li_{0.1}Co_{0.9}V_2O_4$, (d)$Li_{0.2}Co_{0.8}V_2O_4$ with the experimentally obtained hysteresis curve(colored line).

we found α to be 89.5^o. Therefore it is evident that H lies close to the hard axis. This explains the low coercivity and smaller hysteresis loop of theses samples at 300K. Parameters like H_c and M_r depends on angle α whereas M_s is an intrinsic quantity and does not depend on the orientation of the magnetic field[35].

Here the calculation of K_{eff} requires the M_s value but the experimentally obtained hysteresis loop does not show saturation value. The saturation is an intrinsic property and is determined only by the composition of the materials. It is the measure of total number of magnetic moments in a

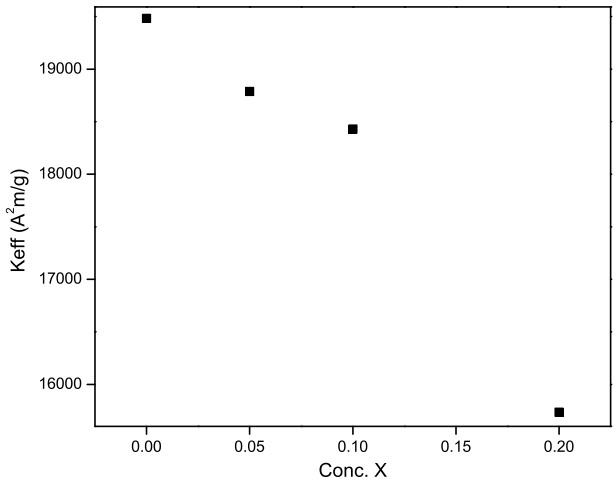

Figure 4.11: The variation of K_{eff} versus the concentration of Li in $Li_xCo_{1-x}V_2O_4$ where x=0,0.05,0.1 and 0.2.

system and is temperature independent while the coercivity is sensitive to structural variables rather than composition[45]. This is why the M_s value for the calculation of K_{eff} is used from the hysteresis loop obtained at 80K. The obtained value of K_{eff} is given in Table 4.6 and the variation of K_{eff} versus the Li dopant concentration is shown in Fig. 4.11. The effective anisotropy energy decreases with the increase in dopant Li concentration. The materials with small anisotropy can be attributed to broad domain walls which makes domain wall movement easy. Anisotropy energies are usually of the range 10^2-10^7 Jm^{-3}. It is larger in matrices with low symmetry and smaller in higher symmetry matrices[7].

The structural and magnetic characterization in Li doped CoV_2O_4 has been successfully studied. The crystal structure has been identified as face center cubic crystal which remains undisturbed for $Li_xCo_{1-x}V_2O_4$. Upon

Table 4.5: The obtained M_s, H_c, M_r of the simulated and experimental magnetic hysteresis of $Li_xCo_{1-x}V_2O_4$ at 300K and 80K.

x	M_r (emu g^{-1})	H_c (Oe)	M_r (emu g^{-1})	H_c (Oe)	M_s (emu g^{-1})	M_r (emu g^{-1})	H_c (Oe)
	10^{-2}	.	10^{-3}				
	expt. 300K		sim.300K		expt.80K		
CoV_2O_4	1.7	295.8	9.6	299.6	33.76	23.75	1017.25
$Li_{0.05}Co_{0.95}V_2O_4$	68.6	463.8	9.4	381.1	30.21	20.95	782.62
$Li_{0.1}Co_{0.92}O_4$	1.2	331.5	9.6	341.3	25.92	14.97	334.42
$Li_{0.2}Co_{0.8}V_2O_4$	1.3	353.1	9.8	359.2	21.35	6.35	129.04

Table 4.6: Obtained parameters from SW simulation and calculation of K_{eff}.

Sample	α	H_k10^5 (A/m)	Ms (emu)	sample weight (g)	Ms/g (Am^2/g)	$K_{eff}10^3$ (A^2m/g)
			10^{-1}	10^{-2}	10^{-3}	
CoV_2O_4	89.5^o	11.54	4.39	1.30	33.76	19.483
$Li_{0.05}Co_{0.95}V_2O_4$	89.5^o	12.44	4.41	1.46	30.21	18.788
$Li_{0.1}Co_{0.9}V_2O_4$	89.5^o	14.22	4.90	1.89	25.92	18.430
$Li_{0.2}Co_{0.8}V_2O_4$	89.5^o	14.74	3.65	1.71	21.35	15.735

doping the lattice parameter of the crystal system decreases also the frequency of modes of vibration changes as a result of change in the crystal environment of $Li_xCo_{1-x}V_2O_4$. An isotropic paramagnetic interaction at 300K is observed which upon doping introduces a uniaxial anisotropy. Also a ferromagnetic interaction at both 300K and 80K is observed. Similarly Co doped Bi_2Se_3 will be studied in the next section in structural and magnetic characterization of $Bi_{2-x}Se_3Co_x$.

Chapter 5

Doping of Co ion in Bi_2Se_3

5.1 Structural characterization

The topological insulator(TI) Bi_2Se_3 doped with Co, $Bi_{2-x}Se_3Co_x$ where x is 0, 0.05 and 0.06, is examined in this chapter. A topological insulator has protected surface states which can be altered by a magnetic impurity. Co is a transition metal doped as a magnetic impurity in Bi_2Se_3 matrix. Doping can lead to novel physical phenomena in TIs. The influence of Co ion in $Bi_{2-x}Se_3Co_x$ is investigated with the help of different spectroscopic techniques like XRD, Raman and FT-IR spectroscopy for structural characterization.

5.1.1 X-Ray diffraction

The XRD pattern of Bi_2Se_3 shown in Fig. 5.1(1). The maximum intensity peak occurs at around 29^o corresponding to (015) crystal plane. The peaks appearing at 18.36^o, 24.73^o, 29.17^o, 38.47^o, 43.40^o, 47.43^o, 53.25^o, 57.31^o,

60.68^o, 66.36^o, 71.03^o, 74.90^o correspond to crystal plane (101), (015), (0012), (1010), (110), (0015), (205), (1016), (0210), (1115), (125) and (1211) respectively. The obtained peaks are in good agreement with JCPDS file no. 33-0214 of Bi_2Se_3[55]. The pattern corresponds to the rhombohedral crystal structure of space group D_{3d}^5 ($R\bar{3}$)m. Bi_2Se_3 is represented as a stack of hexagonally arranged atomic planes, each consisting of only one type of atom arranged in three Se-Bi-Se-Bi-Se sequence making a unit cell[25, 31]. The lattice parameter of rhombohedral crystal structure with hexagonal unit cell is calculated using the formula

$$\frac{4\sin^2\theta}{\lambda^2} = \frac{4}{3}\frac{(h^2+hk+k^2)}{a^2} + \frac{l^2}{c^2}$$

where λ is the wavelength of incident Cu X-ray radiation which is 1.54 $\dot{A}$ and *(hkl)* are the Miller indices of the crystal plane. In hexagonal system there are 3 lattice parameter *a*, *b*, *c* such that $a{=}b{\neq}c$. The angle between a and c(β)=90^o, angle between b and c(α)=90^o and angle between a and b(γ)=120^o. From the literature [49] using the above equation the lattice parameter *a* can be calculated using the (*hkl*) values where *l* is zero. Similarly to find lattice parameter *c*, (*hkl*) values where *h* and *k* are zero can be used. The lattice parameter for Bi_2Se_3 is found to be $a{=}4.163\dot{A}$ and $c{=}28.039\dot{A}$. The XRD pattern of $Bi_{2-x}Se_3Co_x$ is shown in Fig. 5.1(2). The obtained $2\theta^o$ and corresponding (*hkl*) with the calculated lattice parameter *a* and *c* are given in Table 5.1. The XRD peaks of $Bi_{2-x}Se_3Co_x$ are similar to that of undoped Bi_2Se_3 where peaks appear at similar 2θ values. In Fig. 5.1(2) no new peak arises in $Bi_{2-x}Se_3Co_x$ which indicates the undisturbed crystalline nature of

samples on doping. Moreover the absence of (101) plane in doped samples in Fig. 5.1 (b)(c) reveals that the intercalation of Co occurs through the removal of the (101) plane[69]. Upon doping Co ion into the host Bi_2Se_3 the

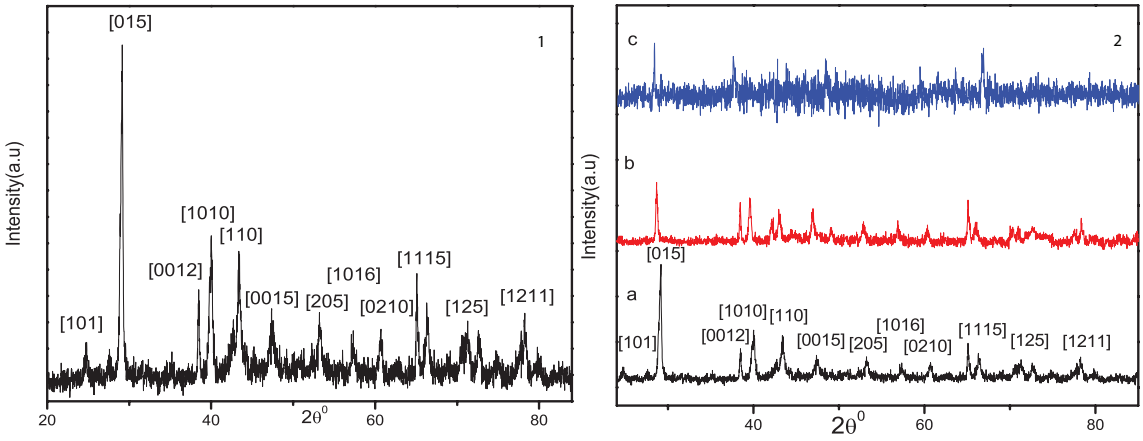

Figure 5.1: XRD pattern of (1)Bi_2Se_3 and (2)(a)Bi_2Se_3 (b)$Bi_{1.95}Se_3Co_0.05$ (c)$Bi_{1.94}Se_3Co_0.06$.

(015) plane peak shifts towards lower θ^o value suggesting the change in lattice parameter. The plot of lattice parameter versus the Co dopant concentration is shown in Fig. 5.2. It can be seen that the presented Co doped system of Bi_2Se_3 has increased crystal lattice parameter compared to the undoped Bi_2Se_3. The lattice spacing a and c both increases upon increasing dopant concentration in $Bi_{2-x}Se_3Co_x$. This is attributed to intercalation of Co ions between Se-Se and Bi-Se ions placing them further apart. The linear fitting of the two lattice parameter a,c was done using the formula a=mx+C. x is the dopant concentration, m is the slope and C is the intercept of the fit. The slope, m gives the rate of change of lattice parameter a when x changes from 0-0.06 where C gives the value of lattice parameter while the crystal is undoped. From the fit the value of m was found to be 0.855($\pm$0.196) and C

Table 5.1: The obtained peak position in $2\theta^o$, calculated lattice parameter, a and c and Miller indices *(hkl)* of $Bi_{2-x}Se_3Co_x$ where x=0, 0.05 and 0.06.

Bi_2Se_3			$Bi_{1.95}Se_3Co_{0.05}$			$Bi_{1.94}Se_3Co_{0.06}$			
$2\theta^o$	a	c	$2\theta^o$	a	c	$2\theta^o$	a	c	*(hkl)*
	$(\dot{A})$	$(\dot{A})$		$(\dot{A})$	$(\dot{A})$		$(\dot{A})$	$(\dot{A})$	
18.36		28.950							006
24.73									101
29.17			28.655			28.419			015
38.47		28.039		28.072	28.072	37.76		28.541	0012
43.40	4.163		42.16	4.198		43.84	4.219		110
47.43		28.705	47.009		28.949	48.41		28.160	0015
53.25			52.869						205
57.31			56.90						1016
60.68			60.34						0210
66.36			66.012			66.89			1115
71.03			70.602						125
74.90									0216

was found to be 4.162($\pm$0.009). For lattice parameter c, m and C was found to be 0.732($\pm$0.089) and 28.038($\pm$0.004). The lattice parameters of the unit cell and peak intensity of (015) plane is given in Table 5.2.

Fig. 5.3(c) is the plot of (015) plane intensity versus the dopant concentration of Co in $Bi_{2-x}Se_3Co_x$. The (015) plane intensity decreases as Co concentration in $Bi_{2-x}Se_3Co_x$ changes from x=0 to 0.06. The decrease in intensity means reduction in structure factor which suggests that upon doping the electron density changes and the phase of reflected waves from the electrons create a destructive Interference[57]. The results show that dopant do not change the polycrystalline nature of the crystal but affects the lattice parameter and the structure factor of the crystal[70]. Using XRD we have identified the rhombohedral crystal nature of $Bi_{2-x}Se_3Co_x$. The influence of dopant Co ion in $Bi_{2-x}Se_3Co_x$ for the concentration x=0, 0.05 and 0.06 is

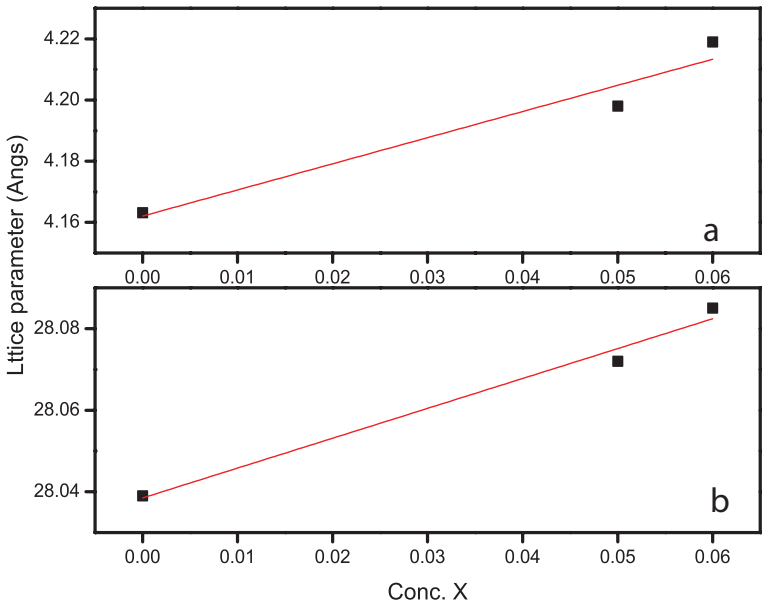

Figure 5.2: Lattice parameter (a)a and (b)c versus the concentration of $Bi_{2-x}Se_3Co_x$ for x changing from 0, 0.05 and 0.06.

Table 5.2: Calculated lattice parameter a and c $(\dot{A})$ and obtained Maximum peak intensity [015] plane of $Bi_{2-x}Se_3Co_x$.

sample	Lattice parameter $(\dot{A})$		Max. intensity (a.u)
Bi_2Se_3	4.163	28.039	180.755
$Bi_{1.95}Se_3Co_{0.05}$	4.198	28.072	92.232
$Bi_{1.94}Se_3Co_{0.06}$	4.219	28.085	27.093

also interpreted in terms of lattice parameter and peak intensity. Further the change in lattice parameter and bond lengths can be interpreted using FT-IR and Raman spectral analysis as change in fundamental vibration modes.

5.1.2 Raman and FT-IR spectral analysis

Fig. 5.4(1) is the FT-IR spectrum of Bi_2Se_3. The FT-IR spectrum in the fingerprint region(500-1500cm^{-1}) show two peaks in Bi_2Se_3. The FT-IR

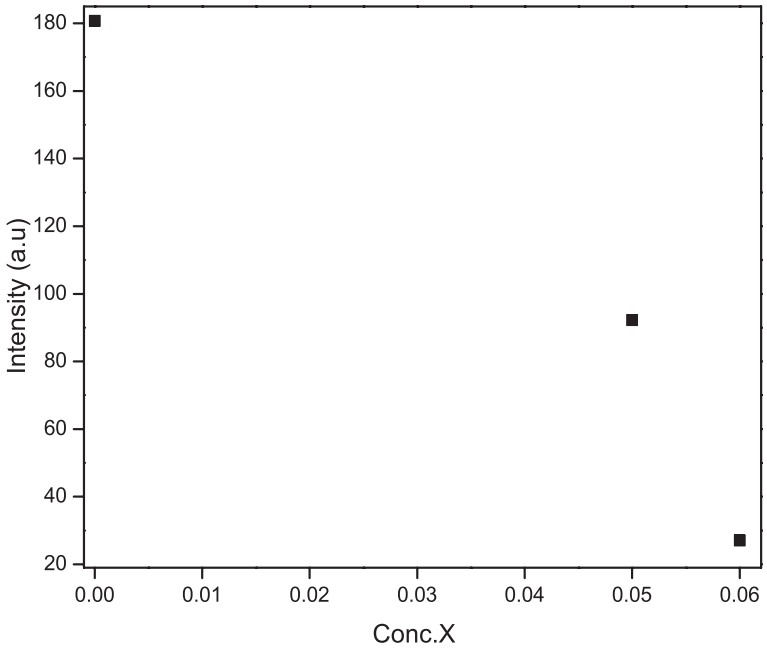

Figure 5.3: Peak intensity of *(015)* plane versus the concentration of $Bi_{2-x}Se_3Co_x$ for x changing from 0, 0.05 and 0.06.

spectra of Bi_2Se_3 has four IR active modes, only two peaks are observed in IR spectrum of Bi_2Se_3. The broad peak in 1000-1200cm^{-1} might have masked the IR peaks due to which only two of them could be seen. The same peaks appear in the doped $Bi_{1-x}Se_3Co_x$ which is an evidence of fingerprint of Bi_2Se_3. Fig. 5.4(2) show the FT-IR spectra of (a)Bi_2Se_3, (b)$Bi_{1.95}Se_3Co_{0.05}$, (c)$Bi_{1.94}Se_3Co_{0.06}$. The substitution of dopant Co in $Bi_{2-x}Se_3Co_x$ for x= 0.05 and 0.06, new peaks appears between 1200-1800cm^{-1}. The new peaks are attributed to the vibrations related to the Co ion in the Bi_2Se_3 matrix. Also in the functional group region (1500-4000cm^{-1}) OH absorption peak appears for $Bi_{2-x}Se_3Co_x$. Upon doping Co, $Bi_{2-x}Se_3Co_x$ adsorbs water and becomes hygroscopic therefore we start seeing an OH intensity peak in FT-IR spectra[71, 72]. Due to the instrument limitation we were not been able to

Table 5.3: Raman shift and peak Intensities of $Bi_{2-x}Se_3Co_x$ for x= 0, 0.05 and 0.06.

Bi_2Se_3		$Bi_{1.95}Se_3Co_{0.05}$		$Bi_{1.94}Se_3Co_{0.06}$		
position	strength	position	strength	position	strength	Assigned
(cm^{-1})	(a.u)	(cm^{-1})	(a.u)	(cm^{-1})	(a.u)	peaks
127.27	0.339	128.45	0.741	122.51	0.535	E_g^2[28]
170.44	0.328	170.38	0.641	164.49	0.408	A_{1g}^2[11]
		233.41	0.120	231.28	0.795	

observe the low energy vibrations due to the heavy metal ions which usually occur below 600cm^{-1}. This is why Raman spectroscopy on $Bi_{2-x}Se_3Co_x$ has been performed to identify the molecular metal ion vibrations.

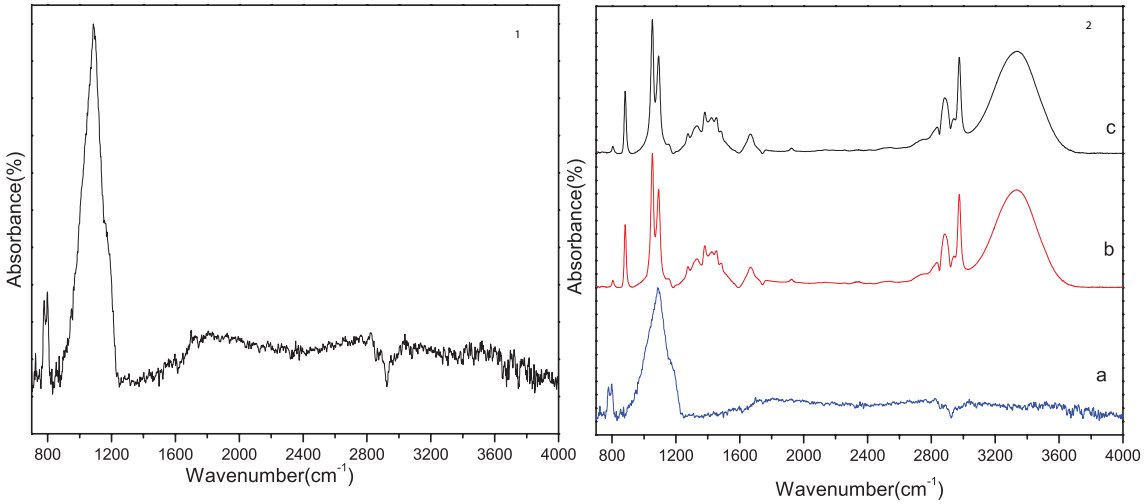

Figure 5.4: FT-IR spectra of (1)Bi_2Se_3 and (2)(a)Bi_2Se_3 (b)$Bi_{1.95}Se_3Co_0.05$ (c)$Bi_{1.94}Se_3Co_0.06$.

Fig. 5.5(1) show the Raman spectrum of Bi_2Se_3. The Raman spectrum of Bi_2Se_3 displays two distinct Raman peaks at 127.27cm^{-1} and 170.44cm^{-1}. Bi_2Se_3 has five atoms in its unit cell and, correspondingly, 15 phonon branches. Twelve of those 15 branches are optical phonons, while the remaining 3 are acoustic phonons. From 12 optical phonons zone center group theory pre-

dicts the Bi_2Se_3 has 4 Raman active and 4 IR active phonon modes. Given by irreducible representation as

$$\Gamma = 2E_g + 2A_{1g} + 2E_u + 2A_{1u}$$

where E_g and A_{1g} are raman active while E_u and A_{1u} are IR active. where E_g and E_u represents the shear mode with in-plane atomic displacements while A_{1u} and A_{1g} describe a breathing mode with out-of plane atomic displacements. In Bi_2Se_3 two Raman active mode E_g^2 and A_{1g}^2 are observed. The Raman peaks at 127.27cm^{-1} and 170.44cm^{-1} correspond to E_g^2 and A_{1g}^2 respectively. The E_g modes is due to the weak Van der Waals interlayer interaction of the quintuple layer of Bi_2Se_3. Such modes are absent in single layered samples [28, 11, 27]. In Fig. 5.5(2) Raman spectra of $Bi_{2-x}Se_3Co_x$ for x= 0.05, 0.06 is shown. The Raman peaks 127.27cm^{-1} and 170.44cm^{-1} are prominent in both the doped $Bi_{2-x}Se_3Co_x$. A new peak corresponding to Co vibration appears at 233cm^{-1} for x= 0.05 then shifts towards lower wavenumber that is 231.28cm^{-1} for x=0.06. This shift can be attributed to increase in concentration of Co in $Bi_{2-x}Se_3Co_x$ matrix which effects the local environment of Bi_2Se_3 and there by changing the interactions. The obtained Raman peaks and their intensities for $Bi_{2-x}Se_3Co_x$ is given in Table 5.3. The lattice parameter a and c of $Bi_{2-x}Se_3Co_x$ varies when the interaction upon doping Co in $Bi_{2-x}Se_3Co_x$ matrix changes. Also the Raman vibrational frequencies are effected as the dopant Co changes the local environment in $Bi_{2-x}Se_3Co_x$. The interaction of Co ion in $Bi_{2-x}Se_3Co_x$ is further investigated in the magnetic characterization of $Bi_{2-x}Se_3Co_x$.

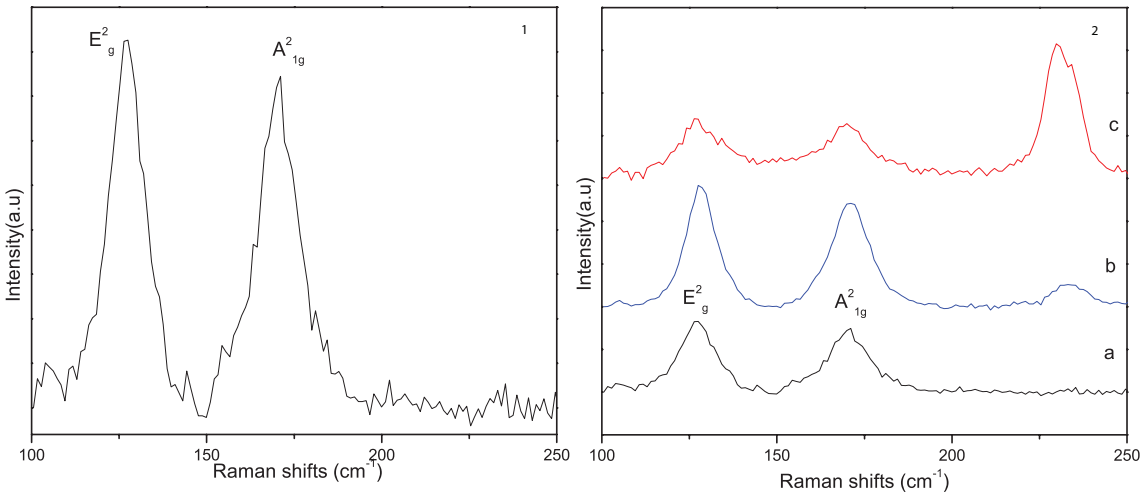

Figure 5.5: Raman spectra of (1)Bi_2Se_3 and (2)(a)Bi_2Se_3 (b)$Bi_{1.95}Se_3Co_0.05$ (c)$Bi_{1.94}Se_3Co_0.06$.

5.2 Magnetic characterization

The magnetic impurities are known to affect the surface states in Bi_2Se_3 and induce surface band gap and ferromagnetism. The $Bi_{2-x}Se_3Co_x$ for x=0,0.05 and 0.06 is examined using SQUID and EPR at two different temperatures, 300K and 80K. The SW model of utilized to analyze the magnetic behaviour of $Bi_{2-x}Se_3Co_x$ at 300K.

5.2.1 EPR spectroscopy

Fig. 5.6(a) is the EPR spectrum of Bi_2Se_3 at 300K where the field is scanned between 80mT to 586mT. The spectrum is also been simulated using an easyspin software and the simulated spectrum is also shown in the same figure. No EPR peaks for Bi_2Se_3 in the scanned range between 86 mT to 586 mT has been observed. The absence of EPR signal is an evidence of missing paramagnetic interaction in Bi_2Se_3. As EPR spectroscopy is sensitive only

to the interaction of unpaired electron with the magnetic field. At 80K no EPR peaks of Bi_2Se_3 were observed as the paramagnetic interactions of neighbouring spins at low temperatures are masked by the exchange and dipole-dipole interaction in the crystal system[1].

The g anisotropy which gives the multiplicity of the energy state of the spin during zeeman splitting is E=gβ_eB. Where B is the magnetic field,β_e is the bohr magneton. The information of the anisotropy is provided in g value of that system such that g_{xx}=g_{yy}=g_{zz} is for isotopic system and g_{xx}=g_{yy}≠g_{zz} for uniaxial anisotropy. In Fig. 5.6(b) the EPR spectra of $Bi_{2-x}Se_3Co_x$ for x= 0.05 is shown. An EPR peak for g=2.16 and 2.1 with S=1/2 is observed. The obtained g>g_e which is the g anisotropy of free electron. g>g_e suggests the paramagnetic species is not a free but trapped in the crystal environment. The obtained parameters are tabulated in Table 5.4. The obtained g value is of the form g_{xx}=g_{yy}≠g_{zz} corresponding to a uniaxial anisotropy in the crystal system. The uniaxial anisotropy introduced in $Bi_{2-x}Se_3Co_x$ could be due to the inhomogeneity in the crystal system upon doping. Fig. 5.6(c)is the EPR spectra of $Bi_{2-x}Se_3Co_x$ for x=0.06. An EPR peak of spin 1/2 for g=2.18 and 2.1 in the same magnetic field of range 86 mT to 586 mT is observed. The uniaxial anisotropy along g_{xx}=g_{yy} increases with increase in Co concentration while g_{zz} remains constant. It suggests that the substitution of Co occurs along two xy plane. Also upon doping Co ion in $Bi_{2-x}Se_3Co_x$ an enhancement of paramagnetic interaction is observed in the crystal environment. The linewidth of the observed EPR signal of $Bi_{2-x}Se_3Co_x$ is about 145mT which arises due to the interaction of dopant ion with the crystal environment.

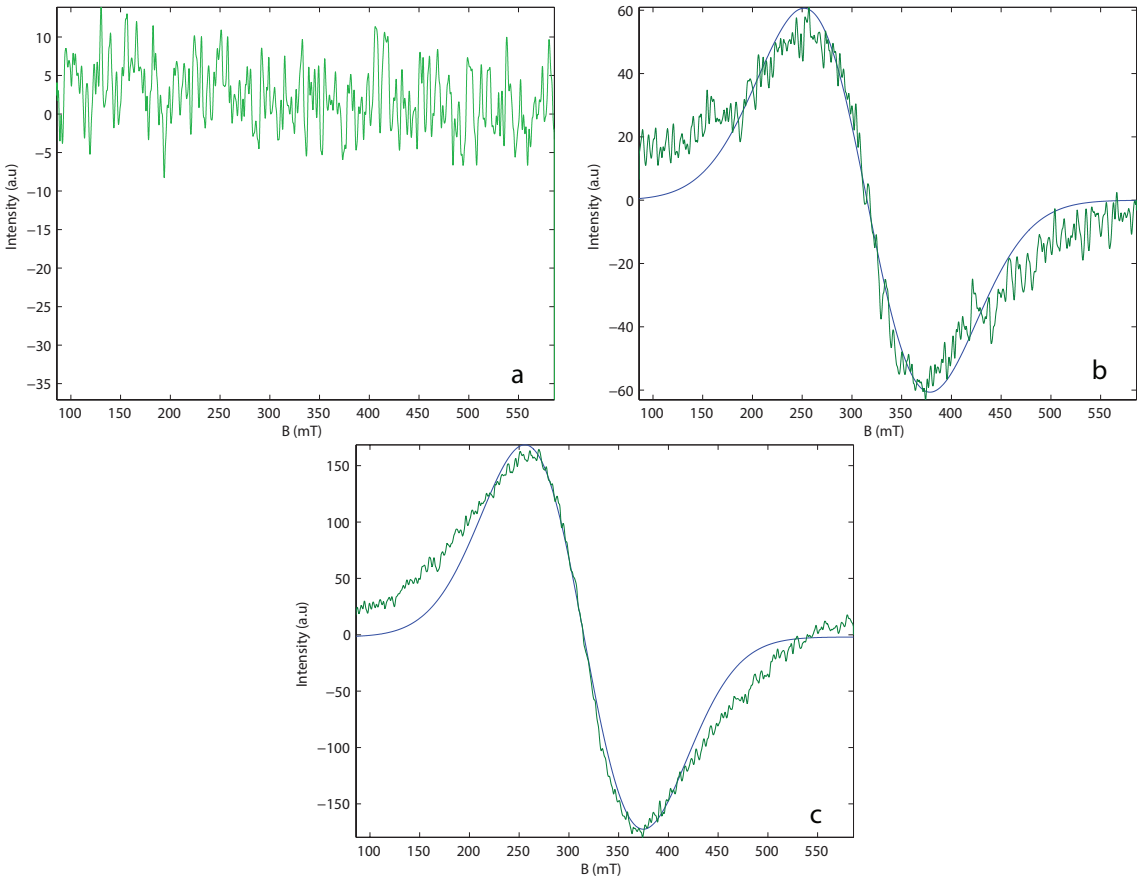

Figure 5.6: EPR spectra of experimental(green line) and simulated(blue line)(a)Bi_2Se_3 (b)$Bi_{1.95}Se_3Co_0.05$ (c)$Bi_{1.94}Se_3Co_{0.06}$ at room temperature,300K.

The lifetime of the spin state can be given as

$$\triangle E.\triangle t \geq \hbar$$

where $\triangle$E is the difference in energy between two spin states, $\triangle$t lifetime of the spin state and $\hbar$ angular momentum of the spin. The obtained lifetime are tabulated in Table 5.4. The obtained lifetime of $Bi_{2-x}Se_3Co_x$ at 300K are 3.6×10^{-11}s for x=0.05 and 3.8×10^{-11}s for x=0.06. $Bi_{2-x}Se_3Co_x$ posses a

Table 5.4: Obtained g value, spin integral, linewidth and lifetime of $Bi_{2-x}Se_3Co_x$.

sample	spin	g value			Linewidth	Lifetime
		g_{xx}	g_{yy}	g_{zz}	mT	10^{-11} s
Bi_2Se_3						
$Bi_{1.95}Se_3Co_{0.05}$	1/2	2.16	2.16	2.1	149	3.6
$Bi_{1.96}Se_3Co_{0.06}$	1/2	2.18	2.18	2.1	140	3.8

uniaxial anisotropy at 300K while at 80K no EPR peaks are seen suggesting the enhanced exchange interaction at this temperature.

The EPR spectra revealed the magnetic behaviour of $Bi_{2-x}Se_3Co_x$ at room temperature as well as low temperature. The magnetic behaviour can be further investigated by plotting the magnetic hysteresis curve. SQUID magnetometry is utilized to obtain the magnetic hysteresis of $Bi_{2-x}Se_3Co_x$ at both 300K and 80K. Also a mathematical SW model is used in order to simulate the obtained hysteresis at 300K.

5.2.2 SQUID magnetometry

Fig. 5.7(a) is the hysteresis curve for Bi_2Se_3 at 300K. The hysteresis curve was obtained while varying applied magnetic field, H between +2000 Oe to -2000 Oe. Magnetization saturates in the applied field region revealing all the magnetic moments are aligned in the direction of the applied magnetic field. The experimentally obtained saturation magnetization,M_s coercivity,H_c and remnant magnetization,M_r for Bi_2Se_3 are found to be 1.02×10^{-3} emu g^{-1}, 67.36 Oe and 1.2×10^{-4} emu g^{-1} respectively. Fig. 5.7(a) is the hysteresis curve of Bi_2Se_3 taken at 80K where applied field ranges from +2000 Oe to -2000 Oe. The M_s, H_c and M_r obtained are 1.08×10^{-3} emu g^{-1}, 91.37 Oe and 1.8×10^{-4}emu g^{-1}. At the same applied range of magnetic field we get more M_s as compared to 300K this could be due to domain freezing at 80K.

The presence of H_c and M_r at both temperatures show that Bi_2Se_3 is ferromagnetic. The increased H_c and M_r at 80K is attributed to strong ferromagnetic interactions between the domains of Bi_2Se_3 at lower temperature.

Fig. 5.8(1) is the hysteresis curve of $Bi_{2-x}Se_3Co_x$ for x=0 to 0.06. The H_c and M_r of the doped and undoped samples are given in Table 5.5. On doping Co in $Bi_{2-x}Se_3Co_x$ there is a small change in H_c and M_s of $Bi_{2-x}Se_3Co_x$ suggesting the change in anisotropy with dopant ion. Fig. 5.8(2) show the hysteresis curve of $Bi_{2-x}Se_3Co_x$ for x=0.05 and 0.06 at 80K. The observed H_c and M_r are larger as compared to 300K which can be attributed to enhanced ferromagnetic interaction of $Bi_{2-x}Se_3Co_x$ at 80K. At this temperature it can be seen from Table 5.5 H_c increases with increasing Co concentration from 0-0.06. The low coercivity in $Bi_{2-x}Se_3Co_x$ can be attributed to easily favourable

domain walls movement which is a property of a soft magnetic material.

From the EPR studies we found that $Bi_{2-x}Se_3Co_x$ shows a uniaxial anisotropy as Co is intercalated into it. The SW model of magnetic hysteresis for uniaxial and single magnetic domain is utilized to simulate the magnetic hysteresis at 300K. The total energy from SW simulation is given by equation

$$E(\phi) = \sin^2(\alpha - \phi) - h\cos\phi$$

Where h=H/H_k and anisotropy field $H_k = 2K_{eff}/M_s$. Effective anisotropy energy density K_{eff} can be calculated by the relation.

$$K_{eff} = \frac{M_s H_k}{2} \tag{5.1}$$

The parameters ϕ is the angle between the magnetization M and applied field H and α is the angle between H and easy axis. For SW simulation α and H_k are the two required fitting parameters. The SW model reconstructs the hysteresis curve which is plotted as a function of cosϕ with H where ϕ is the angle obtained during energy minimization. Fig. 5.9(a) is the simulated and experimental hysteresis curve of Bi_2Se_3. The obtained α and H_k for Bi_2Se_3 is 81.85^o and 31.85×10^3 Oe respectively. The coercivity H_c and remnant magnetization M_r are given in Table 5.6. Fig.5.9(b,c) is the plot of the simulated and the experimental hysteresis curve of Co doped $Bi_{2-x}Se_3Co_x$ for x=0.05 and 0.06. The fitting parameter H_k= 31.85×10^3 is kept constant for the undoped and doped $Bi_{2-x}Se_3Co_x$ while α for Bi_2Se_3 81.85^o increases to

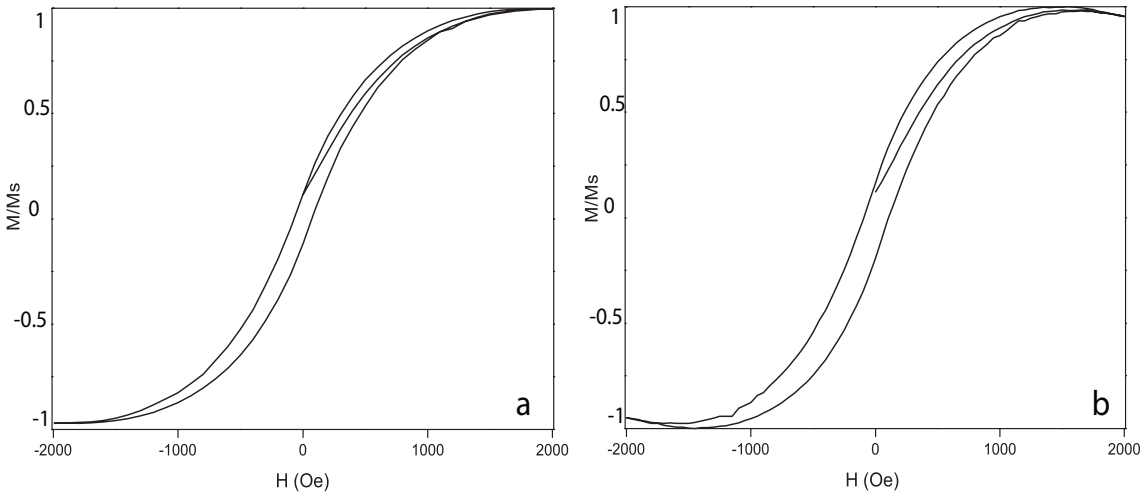

Figure 5.7: The hysteresis curve of Bi_2Se_3 at 300K(a) and 80K(b).

Table 5.5: The obtained M_s, H_c and M_r of the simulated and experimental magnetic hysteresis of at $Bi_{2-x}Se_3Co_x$ at 300K and 80K.

x	M_s	M_r	H_c	M_r	H_c	M_s	M_r	H_c
	10^{-3}	10^{-4}		10^{-1}		10^{-3}	10^{-4}	
	($emug^{-1}$)		(Oe)	($emug^{-1}$)	(Oe)	($emug^{-1}$)		(Oe)
	expt. 300K			sim.300K		expt.80K		
Bi_2Se_3	1.02	1.2	67.36	1.38	114.3	1.08	1.8	91.37
$Bi_{1.95}Se_3Co_{0.05}$	0.45	0.2	22.47	1.19	106.8	1.05	7.7	217.17
$Bi_{1.94}Se_3Co_{0.06}$	0.85	0.7	41.25	1.20	95.69	3.79	24.0	610.42

82.55^o and 83.06^o for $Bi_{1.95}Se_{0.05}$ and $Bi_{1.94}Se_{0.06}$ respectively. The increase in α suggests the alignment of magnetic field approaches towards the hard axis. H_c decreases when dopant Co_x changes from 0-0.06 at 300K. H_c and M_r depends on angle α thus the decrease in the coercivity of the hysteresis curve can be interpreted as the alignment of the H close to hard axis. The effective anisotropy energy K_{eff} results from the shape and magnetocrystalline anisotropy energy of the system. K_{eff} of $Bi_{2-x}Se_3Co_x$ can be calculated using the formula $M_sH_k/2$. The total magnetic moment can be measured from the M_s obtained at 300K assuming all the moments are aligned along the direction

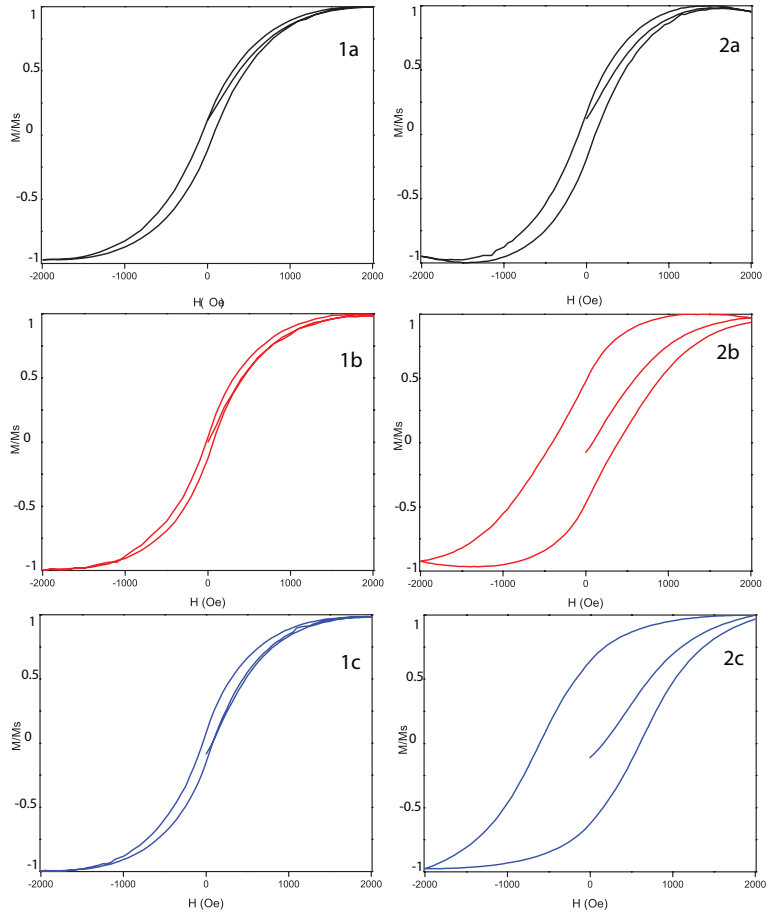

Figure 5.8: The hysteresis curve of $Bi_{2-x}Se_3Co_x$ at 300K(1) and 80(K)(2).

of H as compared to those at 80K. Therefore M_s value obtained for 300K is utilized for the calculation of K_{eff}. The fitting parameters from the simulation and calculated K_{eff} is given in Table 5.6. The obtained K_{eff} and H_c of the material is small which indicates $Bi_{2-x}Se_3Co_x$ to be highly symmetric[7]. The K_{eff} of $Bi_{2-x}Se_3Co_x$ is found to be constant around 12.33×10^{-3} Am^2/g. The K_{eff} versus the Co concentration in $Bi_{2-x}Se_3Co_x$ is shown in Fig. 5.10. Bi_2Se_3 has a time reversal symmetry it is theoretically predicted that the cobalt ions on being adsorbed on the surface of Bi_2Se_3 would exhibit a fer-

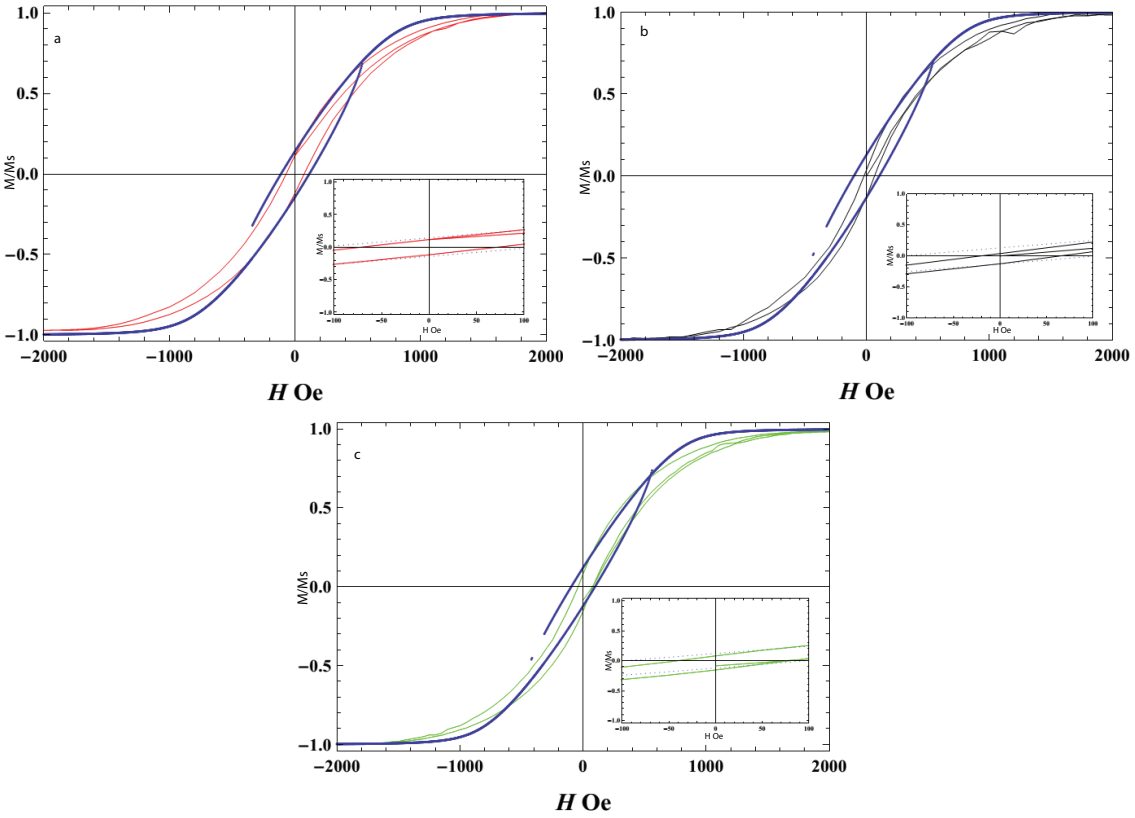

Figure 5.9: Hysteresis curve of SW simulated(blue line) and experimentally obtained(colored line)(a)Bi_2Se_3, (b)$Bi_{1.95}Se_3Co_{0.05}$, (c)$Bi_{1.94}Se_3Co_{0.06}$.

romagnetic coupling with the net magnetic moment aligned perpendicular to the surface plane. These interaction in topological insulator breaks the time reversal symmetry, thus opening a surface band-gap[1]. The property of TI are unique and have a huge application in quantum computation and spintronics[10].

Table 5.6: Obtained parameters from SW simulation and calculation of K_{eff}.

Sample	α	$H_k 10^3$ (A/m)	Ms 10^{-5} (emu)	sample weight (g)10^{-2}	Ms/g 10^{-4} (Am^2/g)	K_{eff} 10^{-3} (A^2m/g)
Bi_2Se_3	81.85^o	31.847	3.48	3.41	10.2	16.2
$Bi_{1.95}Se_3Co_{0.05}$	82.55^o	31.847	1.50	3.36	3.3	7.2
$Bi_{1.94}Se_3Co_{0.06}$	83.06^o	31.85	2.86	3.35	8.5	13.6

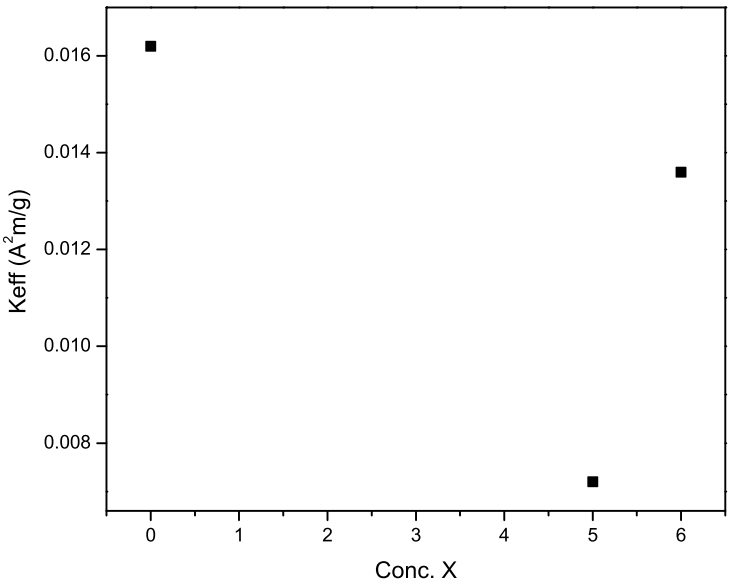

Figure 5.10: The variation of K_{eff} versus the concentration of Co in $Bi_{2-x}Se_3Co_x$.

Part IV

5.3 Conclusion and future prospects

The major contributions of the research work presented in this thesis are summarized in this section. The brief details of results obtained and conclusions which have been drawn are listed with the future prospects.

5.3.1 Conclusion

5.3.2 $Li_xCo_{1-x}V_2O_4$

Structural Characterization

It has been observed the crystal structure of $Li_xCo_{1-x}V_2O_4$ is a FCC crystal. The crystal structure remains undisturbed under the concentration x changing from 0 to 0.2 in $Li_xCo_{1x}V_2O_4$ while the lattice parameter and vibrational properties are modified. The reduction in lattice parameter is attributed to the decrease in coulomb repulsion in the crystal environment of $Li_xCo_{1-x}V_2O_4$.

Magnetic characterization

The magnetometry studies show $Li_xCo_{1-x}V_2O_4$ is paramagnetic at 300K. The dopant introduces a uniaxial anisotropy in isotropic paramagnetic media. Whereas in 80K other interactions such as exchange interaction dominate. The presence of room temperature ferromagnetism(RTFM) is also confirmed in $Li_xCo_{1-x}V_2O_4$. The exchange interaction are enhanced upon lowering the temperature.

5.3.3 $Bi_{2-x}Se_3Co_x$

Structural Characterization

The crystal structure of $Bi_{2-x}Se_3Co_x$ crystallize in rhombohedral crystal system. The crystal structure remains undisturbed under the concentration x changing from 0 to 0.06. The change in lattice parameter and vibrational properties are observed. The increase in lattice parameters are attributed to the insertion of Co ions between the Bi-Se and Se-Se quintuple layers.

Magnetic characterization

The magnetometry studies show $Bi_{2-x}Se_3Co_x$ is paramagnetic for x=0.05 and 0.06 at 300K. The dopant introduces a uniaxial anisotropy in $Bi_{2-x}Se_3Co_x$. Whereas in 80K do not show paramagnetic behaviour. The presence of room temperature ferromagnetism(RTFM) is observed in $Bi_{2-x}Se_3Co_x$. The exchange interaction are enhanced at 80K.

T he intercalation of Li in $Li_xCo_{1-x}V_2O_4$ and Co in $Bi_{2-x}Se_3Co_x$ do not affect the crystal structure. The modifications are seen in lattice parameters and molecular vibrational modes. Similar to $Li_xCo_{1-x}V_2O_4$ in $Bi_{2-x}Se_3Co_x$ paramagnetic interaction are observed at 300K whereas at 80K other interactions dominate masking the paramagnetic interaction. In both the cases a uniaxial anisotropy is introduced in the matrix due to the dopant. Further the RTFM is observed in both the samples. The presence of RTFM can be attributed to the anisotropic energy arising in the material upon doping. A SW model which holds good for single domain, uniaxial anisotropy is im-

plied in both of the systems. The basic parameters such as Coercive field,H_c, magnetization,M_r,M_s, effective energy density,K_{eff}, anisotropy field,H_k and easy axis are obtained. It is also observed that large anisotropy is prevalent in $Li_xCo_{1-x}V_2O_4$ of the order of 10^3 which gradually decreases with increasing dopant concentration. Whereas in $Bi_{2-x}Se_3Co_x$ the anisotropy energy density is of order of 10^{-3} and remains nearly constant upon doping. The RTFM is of great importance in condensed matter application for magnetic refrigeration, also the low H_c corresponds to the soft magnetic materials which are desired for their ability to shape the magnetic flux with high efficiency. $Li_xCo_{1-x}V_2O_4$ at 300K is not a good material for magnetic storage as the M_s can only be achieved for very high applied magnetic field range. On the other hand $Bi_{2-x}Se_3Co_x$ at 300K is a good candidate for magnetic storage application. M_s is attained quickly for low applied magnetic field range, the magnetic reversal or the H_c is small which is good for manipulating the stored data.

5.4 Future Prospects

$Li_xCo_{1-x}V_2O_4$ and $Bi_{2-x}Se_3Co_x$ can be further investigated for their entropy change over wide range of magnetic field. This will help in realizing its potential in RTFM application. Further investigation can be carried out on elastic response of these materials while changing the dopant concentrations. To understand the effect of temperature on the structural and magnetic properties a temperature dependent study of structural and magnetic phase transition can be done. The simulations of room temperature hysteresis has been

performed, the magnetic hysteresis at low temperature using mathematical model can also be studied. The properties of $Li_xCo_{1-x}V_2O_4$ and $Bi_{2-x}Se_3Co_x$ can be further tuned by increasing the dopant concentration. One can observe the change in properties while doping with different ions such as Cr, Mn, Zn etc. in the same parent Bi_2Se_3 and $Co_xV_2O_4$.

5.5 APPENDIX

5.6 Stoner-Wohlfarth simulation programme

Stoner-Wohlfarth simulation programme Sequence command for the magnetisation as a function of applied magnetic field and plot of hysteresis curve at he temperature at 300 K.

h = Table[i, i, -2000, 2000, 5]; α= 1.4278

Needs[”PlotLegends‘”]

c = 2.5×10^{-3} Clear; Buffer = ; For[i = 1, i ¡= Length[h], i++, energy = Plot[(Sin[[α] - [ϕ]])^2 - c*h [[i]] Cos[[ϕ]], [ϕ],

0, 2 [Π], Axes →True, Frame → True,

FrameLabel → h[[i]],

Ticks → 0, π,π2, 3π2, 2π, Automatic];,

AppendTo[Buffer, energy]]; Buffer; Clear; Buffer2 = ;

For[i = 1, i ¡= Length[h],

i++, A =

FindMinimum[

Sin[α - ϕ]^2 - c*h[[i]] Cos[[ϕ]], [ϕ], 0, $\pi/2$],

B = FindMinimum[Sin[[α] - [ϕ]]^2 - c*h[[i]] Cos[[ϕ]], [ϕ], [π], 2[π]], AppendTo[Buffer2, h[[i]], A, B]];

list1 = Flatten[Buffer2]; list2 = Partition[list1, 5]; Clear; Buffer3 = ; For[i = 1, i ¡= Length[list2], i++,

A1 = ToExpression[StringDrop[ToString[list2[[i]][[3]]], 5]],

B1 = ToExpression[StringDrop[ToString[list2[[i]][[5]]], 5]], AppendTo[Buf-

fer3, list2[[i]][[1]], N[Cos[A1]], list2[[i]][[1]], N[Cos[B1]]]]; list3 = Flatten[Buffer3]; list4 = Partition[list3, 2]; hystersis =

ListPlot[list4, Frame → False, Axes → True,

PlotStyle →PointSize[0.005], AxesOrigin → 0, 0]

5.6.1 Conversion

$$C = \frac{1}{H_k} \tag{5.2}$$

$$K_{eff} = \frac{H_k M_s}{2} \tag{5.3}$$

$$1Oe = \frac{10^3}{4\pi}\frac{A}{m} \tag{5.4}$$

$$1emu = 10^{-3} Am^2$$

5.6.2 Important parameters

Parameter	Description	Value
h	applied magnetic field H	Varies from positive to negative field
α	Angle between applied magnetic field and easy axis	Varies with sample
ϕ	Angle between h and magnetization	Varies from 0 and 2π
C=1/HK	Constant and inverse of anisotropy field H_k	Varies with sample

5.7 Easyspin simulation

clear, clf

Exp.mwFreq = 9.44; Exp.Range = [86 586]; Exp.nPoints = 65536; Exp.Harmonic = 1;

Sys = struct('S',1/2,'g',2.15,'n',1,'Nucs','Co','A',115,'lwpp',[10,20]); Sys.gStrain = [0] [B,spec0] = pepper(Sys,Exp);

Sys1 = struct('S',1/2,'g',[2.15],'lw',[400,58]); Sys.gStrain = [0] [B,spec1] = pepper(Sys1,Exp); ModulationAmplitude = 10;

h=plot(B, spec0);

load .dat a=B1(:,2); c=B1(:,1);

y = plot(c,a);

plot(B, spec1*2.8E3+spec0*1.8E3,c,a)

plot(B, spec0, c, a) h = plot(Y/10,spec1+1E5,B,(spec0*6.5E2+spec2*2E6+spec3*1.5E2)); axis([86,586,-inf,inf]) xlabel('magnetic field [mT]');

5.7.1 Important parameters

Parameter	Description	Value
Exp.mwFreq	applied microwave frequency	9.44
Exp.Range	Range applied magnetic field	86mT 586mT
S	spin	1/2
g	Lande' g-factor	Varies with the sample
A	Anisotropy of the sample	Varies with sample

Bibliography

[1] B.Irfan and R.Chatterjee. "Magneto-Transport and Kondo Effect in Cobalt doped Bi_2Se_3 Topological Insulators". *Applied Physics Letters*, 107(173108):1–5, 2015.

[2] Y. Luan. "Elastic Properties of Complex Transition Metal Oxides Studied by Resonant Ultrasound Spectroscopy". *University of Tennessee, Knoxville ,Trace: Tennessee Research and CreativeExchange, Dessertation*, 2011.

[3] L. Hu S.G. Tan Y. Liu B. Yuan J. Chen W.H. Song Z.H. Huang, X. Luo and Y.P. Sun. "Observation Of The Large Magnetocaloric Effect And Suppression Of Orbital Entropy Change In Fe-Doped Mnv_2O_4". *Journal Of Applied Physics*, 115:034903–1–5, 2014.

[4] T. Arima S. Aoyagi R. Sakai S. Maki E. Nishibori H. Sawa K. Sugimoto H. Ohsumi Y. Nii, H. Sagayama and M. Takata. "Orbital structures in spinel vanadates AV_2O_4 (A = Fe, Mn)". *Physical Review B 86*, 12:125142–1–6, 2012.

[5] A.A. Aczel H.D. Zhou S.E. Nagler G.J. MacDougall, V.O. Garlea. "Magnetic order and ice rules in the multiferroic spinel $FeV_2O_(4)$ ". *Physical Review B 86*, (060414(R)):1–8, 2012.

[6] S. Kumar D.K. Dubey D.N. Singh A. Tiwari A. Triphati A.K. Ghosh S. Chatterjee. P. Sahi, R. Singh. "Effect of Lithium on Transport Properties Of $FeV_2O_(4)$ and CoV_2O_4".

[7] S.Blundel. "Mgnetism In Condensed Matter". *Oxford Master Series In Condensed Matter Physics*, 2001.

[8] A. Yoichi. "Topological Insulator Materials". *Journal of the Physical Society of Japan*, pages 1–36, 2013.

[9] J.E. Moore. "The Birth of Topological Insulators". *Nature*, 464(08916):196–198, 2010.

[10] E.J. Walter E.J. Mele C.L. Kane S.M. Young, S. Chowdhury and A. M. Rappe. "Theoretical Investigation of The Evolution of The Topological Phase of Bi_2Se_3 Under Mechanical Strain". *Physical Review B*, 84(8).

[11] V. Goyal K.M.F. Shahil, M.Z. Hossain and A.A. Balandin. "Micro-Raman spectroscopy of Mechanically Exfoliated Few-Quintuple Layers of Bi_2Te_3, Bi_2Se_3, and Sb_2Te_3 Materials". *Journal of Applied Physics*, 111(054305):1–8, 2012.

[12] K. Kato K. Osaka M. Takata K. Adachi, T. Suzuki and T. Katsufuji. "Magnetic-Field Switching of Crystal Structure in an Orbital-Spin-

Coupled System: MnV2O4". *Physical Review Letters*, 95(197202-1-4), 2005.

[13] K. Osaka M. Takata T. Sonehara, K. Kato and T. Katsufuji. "Transport, Magnetic, and Structural Properties of Spinel $MnTi_2O_4$ and The Effect of V doping". *Physical Review B*, 74(104424):1–7, 2006.

[14] Y. Yamashita and K. Ueda. "Spin Driven Jahn-Teller Distortion in a Pyrochlore System". *Physical review letters*, 85(23):4960, 2000.

[15] S. Maat and A.C. Marley. "Physics and Design of Hard Disk Drive Magnetic Recording Read Heads". *Handbook of Spintronics*, Springer Science+Business Media Dordrecht, 2014.

[16] J. Shen B. Gao H.W. Zhang F.X. Hu G.J. Liu, J.R. Sub and B.G. Shen. "Determination Of The Entropy Changes In The Compounds With A First-Order Magnetic Transition". *Applied Physics Letters*, 90:032507–1–3, 2007.

[17] D.Vurnoz M. Diebold C. Besson P.W. Egolf, A. Kitoviski. "An Introduction to Magnetic Refrigeration".

[18] P.A. Joy S. Deka. "Synthesis and Magnetic Properties of Mn Doped ZnO Nanowires". *Solid State Communications*, 142, 2007.

[19] R.M. Kadam P.L. Paulose A.K. Rajarajan T.K. Nath A.K. Das I. Dasgupta D. Karmakar, S.K. Mandal and G. P. Das. "Ferromagnetism in Fe-doped ZnO Nanocrystals: Experimental and Theoretical investigations". *Physical Review B*, 2007.

[20] M.B. Sullivan X. Luo and S.Y. Quek. "First Principles Investigations of the Atomic, Electronic, and Thermoelectric Properties of Equilibrium and Strained Bi_2Se_3 and Bi_2Te_3 with van der Waals Interactions". *Physical Review B*, 86(18):1–35, 2012.

[21] S. Kumar D.K. Dubey D.N. Singh A. Tiwari A. Triphati A.K. Ghosh S. Chatterjee. P. Sahi, R. Singh. "Effect of Dilution of Both A and B sites on the Multiferroic Properties of Spinel Mott Insultors".

[22] H. Ishibashi Y. Hosokoshi X.M. Ren S. Nishihara, W. Doi and S. Mori. "Appearance of Magnetization Jumps in Magnetic Hysteresis Curves in Spinel Oxide FeV_2O_4". 107(09A504):1–3, 2010.

[23] Z. Yang Y. Huang and Y. Zhang. "Magnetic, Structural, and Thermal Properties of CoV_2O_4". *J. Phys.: Condens. Matter*, 24(056003):1–6, 2012.

[24] J. Peng J. Weng Y. Huang L. Sun, Z. Lin and Z. Luo. "Preparation of Few-Layer Bismuth Selenide by Liquid-Phase-Exfoliation and Its Optical Absorption Properties". *Scientific Reports*, 4(4794):1–8, 2014.

[25] B.S. Kim S. Choi J. Choi J. Choi, H.W. Lee and S. Cho. "Single Crystal Growth and Magnetic Properties of Mn Doped Bi_2Se_3 and Sb_2Se_3". *Journal of Magnetics*, 9(4):125–127, 2004.

[26] R.H. Bari and L.A. Patil. "Synthesis and Characterization of Bismuth Selenide Thin Films by Chemical Bath Deposition Technique". *Indian Journal of Pure and Applied Physics*, 48:127–132, 2010.

[27] V. Etgens M. Eddrief, P. Atkinson and B. Jusserand. " Low-temperature Raman Fingerprints for Few-Quintuple Layer Topological Insulator Bi_2Se_3 Films Epitaxied on GaAs". *Nanotechnology*, 8(245701):1–8, 2014.

[28] A.P.S. Gaur M. Ahmadi M. J-F. Guinel R.S. Katiyar B. Irfan, S. Sahoo and R. Chatterjee. "Temperature Dependent Raman Study of Phonons of Different Symmetries in Single Crystal Bi_2Se_3". *Condensed Matteer. Material Science*, 1:1–5, 2014.

[29] J.K. Yoon J.H. Jeon, W.J. Jang and S.J. Kahng. "Metal-Supported HighCrystalline Bi_2Se_3 Quintuple Layers". *Nanotechnology*, 22:1–4, 2011.

[30] S.D. Mahanti S. Urazhdin, D. Bilc and S.H. Tessmer. "Surface Effects in Layered Semiconductors Bi_2Se_3 and Bi_2Te_3". *Physical Review B*, 69(085313):1–7, 2004.

[31] M. Kaminska A. Hruban S.G. Strzelecka-A. Materna M. Piersa M. Romaniec R. Diduszko A. Wolos, A. Drabinska. "Electron Paramagnetic Resonance of Mn in Bi2Se3Topological Insulator". *Journal of The Electrochemical Society.*

[32] A. Kiswandhi I. Miotkowski Y.P. Chen X. Chen, H.D. Zhou. "Thermal Expansion Coefficients of Bi_2Se_3 and Sb_2Te_3 Crystals From 10K to 270K". *Applied Physics Letters*, 99(261912):1–3, 2011.

[33] T. Bdrich J. Ziske. "Magnetic Hysteresis Models for Modelica". *Technische Universitt Dresden, Institute of Electromechanical and Electronic Design*, pages 151–158, 2012.

[34] C. Tannous and J. Gieraltowski. "The Stoner-Wohlfarth Model of Ferromagnetism: Static Properties". *Physics.Class-ph*, 0607117(3):1–11, 2008.

[35] C. Tannous and J. Gieraltowski. "The StonerWohlfarth Model of Ferromagnetism". *European Journal Physics*, 29:475487, 2008.

[36] A. Tiwari T. Mondal, A. Tripathi. "Magnetization reversal of transition metal doped ZnO nanosystems". *Indian journal of pure and applied Physics*, 53:701–704, 2015.

[37] O. Gaier. "A study of Exchange Interaction, Magnetic Anisotropies, and Ion Beam Induced Effects in Thin Films of Co_2-Based Heusler Compounds". *Doctoral thesis*, Oxford 2009.

[38] J.G. Gay and R. Richter. "Spin Anisotropy of Ferromagnetic Films". *Physical Review Letters*, 56(25):2728–2731, 1986.

[39] T.R. Mcguire and R.I. Potter. "Anisotropic Magnetoresistancein Ferromagnetic 3d Alloys". *Sactions on Magnetics*, 11(4):1018–1037, 1975.

[40] J. Tellinen. "A Simple Scalar Model for Magnetic Hysteresis". *IEEE Transactions on Magnetics*, 34(4):2200–2206, 1998.

[41] H. Schmidt. "Magnetization Reversal by Coherent Rotation in Singledomain Magnets with Arbitrary Anisotropy". *Journal of Applied Physics*, 93(4):2107–2112, 2003.

[42] P.R. Gillette and K. Oshima. "Thin Film Magnetization Reversal by Coherent Rotation". *ournal of Applied Physics*, 29(10):1465–1470, 1958.

[43] L.D. Landau and E.M. Lifshitz. "Electrodynamics of Continuous Media". *Pergamon*, page p.157, Oxford 1975.

[44] R.F. Elfant and F.J. Friedlaender. "Approximate Solution of the Equations of Magnetization Reversal by Coherent Rotation". *ournal of Applied Physics*, 33(3):1071–1072, 1962.

[45] C. Tannous and J. Gieraltowski. "Magnetization Process of Noninteracting Ferromagnetic Cobalt Nanoparticles in The Superparamagnetic Regime: Deviation from Langevin law". *Journal of Applied Physics*, 86(1), 1999.

[46] S.Y. Hahn C.S. Koh and G.S. Park. "Vector Hysteresis Modeling by Combining StonerWohlfarth and Preisach Models". *IEEE Transactions on Magnetics*, 36(4):1254–1257, 2000.

[47] R. Singh R. Singh P.U. Sastry-A. Das A.G. Joshi A.K. Ghosh A. Banerjee P. Shahi, A. Kumar and S. Chatterjee. "Effect of Chemical Pressure at the Boundary of Mott Insulator to Itinerant Electron Limit Transition in Spinel Vanadates". *Science of Advanced Materials*, 1947-2935(7):1–10, 2015.

[48] K.J. Lee J.B. Yoon C.Y. You Y.H. Choi, N.H. Jo and M.H. Jung. "Transport and Magnetic Properties of Cr-, Fe-, Cu-Doped Topological insulators". *Journal of Applied Physics*, 0021-8979(109(7)):07E312–1–3, 2011.

[49] S.R. Stock B.D. Cullity. "Elements of X-RAY Diffraction". *Prentice-Hall, Inc.*, (0-201-61091-4), 2001.

[50] McCash E. M. Banwell, C. N. "Fundamentals of Molecular Spectroscopy". *London, McGraw-Hill*, 1972.

[51] F.A. Miller and C.H. Wilkins. "Infrared Spectra and Characteristic Frequencies of Inorganic Ions, Their Use in Qualitative Analysis". *Analytical Chemistry*, 24(8):1253–1294, 1952.

[52] UC Davis. "EPR Interpretation". *http://chemwiki.ucdavis.edu.in*, pages 1–5, 1/14/2016.

[53] J.R. Bolton J.A. Weil. "Electron Paramagnetic Resonance". *Weily-Interscience, A John Weily and Sons, Inc., Publication*, Second Edition, 2007.

[54] M. Rabbani R. Rahimi, M. Bozorgpour. "Synthesis of Fe-doped Nickel Oxide Nanostructures Via a Simple Mechanochemical Route and its Application for Photocatalytic Removing of MB". *ecsoc-17*, (3390-1-8), 2004.

[55] E.H. Evans B. Paretzkin H.S. Parker M.C. Morris, H.F. McMurdie and N.C. Panagiotopoulos. "Standard X-ray Diffraction Powder Patterns". *U.S. Department of Commerce*, Monogr. 25Sec. 18:16, 1981.

[56] G. Chandrasekaran R. Elilarassi. "Synthesis, Structural and Magnetic Characterization of Ni-Doped ZnO Diluted Magnetic Semiconductor ". *American Journal of Materials Science*, 2(1):46–50, 2012.

[57] S.C. Wallwork. "Introduction to Calculation of Structure Factors". *University College Cardiff Press Cardiff, Wales*, 2001.

[58] J. Liu L. Liu S. Liang Y. Tang, J. Zhou. "Facile Synthesis of Cobalt Vanadium Oxides and Their Applications in Lithium Batteries". *Int. J. Electrochem. Sci.*, 8, 2013.

[59] S.J. Hibble P.G. Dickens, A.H. Chlpplndale and P. Lancaster. "Hydrogen Insertion Compounds of V6013 AND V205". *Materials Research Bulletin*, 19(3):319–324, 1984.

[60] G. Busca C. Cristiani, P. Fforzatti. "On the Surface Structure of Vanadia-Titania Catalysts:Combined Laser-Raman and Fourier Transform-Infrared Investigation". *Journal of Catalysis*, 116:586–589, 1988.

[61] T.Hiratat and H.-Y. Zhu. "Identification and Vibrational Properties of The Mixed Oxide (1-x)$V_2O_5 + xMoO_3$ (x 0.3)". *Journal of Physics: Cnndensed Matter*, 4:7377–7388, 1992.

[62] S. Qiu B.L. Hurley and R.G. Buchheit. "Raman Spectroscopy Characterization of Aqueous Vanadate Species Interaction with Aluminum Alloy 2024-T3 Surfaces". *Journal of The Electrochemical Society*, 158(5):c125–c131, 2011.

[63] W.Y Yu C.B Wang C.W Tang, T.Y Leu and S.H Chien. "Characterization of Cobalt Oxides Studied by FT-IR, Raman, TPR and TG-MS". , .

[64] C.J. Kiely and I.E. Wachs K. Routray, W. Zhou. "Catalysis Science of Methanol Oxidation over Iron Vanadate Catalysts: Nature of the Catalytic Active Sites". *American Chemical Society*, 1:55–66, 2010.

[65] A. T. Bell B. Kilos and E. Iglesia. "Mechanism and Site Requirements for Ethanol Oxidation on Vanadium Oxide Domains". *J. Phys. Chem. C*, 113(7):28302836, 2009.

[66] A.M. Turek G.Deo and I. E. Wachs. "Physical and Chemical Characterization of Surface Vanadium Oxide Supported onTtitania: Influence of the Titania Phase". *Applied CatalysisA: General*, 91:27–42, 1992.

[67] R.B. Hadjean and J.P. Ramos. "Raman Microspectrometry Applied to the Study of Electrode Materials for Lithium Batteries". *Chemical Review*, 110(3):12781319, 2010.

[68] E. Zhecheva and R. Stoyanova. "Effect of Allied and Alien Ions on The EPR Spectrum of Mn4C-Containing LithiumManganeseSpinel Oxides". *Solid State Communications 135*, 135:405–410, 2005.

[69] D.P. Padiyan S. Subramanian. "Effect of Structural, Electrical and Optical Properties of Electrodeposited Bismuth Selenide Thin Films in Polyaniline Aqueous Medium". *Materials Chemistry and Physics*, 107:392398, 2007.

[70] F.S. Bahabri. "Investigation of The Structural and Optical Properties of Bismuth Telluride (Bi_2Te_3) Thin Films". *Life Science Journal*, 9(1):290–294, 2012.

[71] Y. Liu and L. Ojame. "Fingerprints in IR OH Vibrational Spectra of H_2O Clusters From Different H-bond Conformations by Means of Quantum-Chemical Computations". *Journal of Molecular Modeling*, 6(20):1–16, 2014.

[72] H.C. Chiu H.K. Lin, C.B. Wang and S.H. Chien. "In Situ FTIR Study of Cobalt Oxides for The Oxidation of Carbon Monoxide". *Catalysis Letters*, 86(1-3):63–68, 2003.